Tuning of Oxygen Electrocatalysis in Perovskite Oxide Nanoparticles by the Cationic Composition

Madeleine Han, Isabel Gómez-Recio, Daniel Gutiérrez Martín, Nathaly Ortiz Peña, Maria Luisa Ruiz-González, Mohamed Selmane, José González-Calbet, Ovidiu Ersen, Andrea Zitolo, Benedikt Lassalle-Kaiser, et al.

Tuning of Oxygen Electrocatalysis in Perovskite Oxide Nanoparticles by the Cationic Composition

Madeleine Han[1,2], Isabel Gómez-Recio,[2] Daniel Gutiérrez Martín,[3] Nathaly Ortiz Peña,[4] Maria Luisa Ruiz-González,[3] Mohamed Selmane,[5] José M. González-Calbet,[3] Ovidiu Ersen,[4] Andrea Zitolo[1], Benedikt Lassalle-Kaiser*[1], David Portehault*[2], Christel Laberty-Robert*[2]

[1] Synchrotron SOLEIL, L'Orme des Merisiers, Départementale 128, 91190, Saint-Aubin, France

[2]Sorbonne Université, CNRS, Laboratoire Chimie de la Matière Condensée de Paris, LCMCP, 4 Place Jussieu, F-75005 Paris, France

[3] Dpto. de Química Inorgánica I, Facultad de Ciencias Químicas, Universidad Complutense, 28040 Madrid, Spain

[4]Institut de Physique et Chimie des Matériaux de Strasbourg (IPCMS), UMR 7504 CNRS − Université de Strasbourg, 23 rue du Loess, BP 43, Strasbourg Cedex 2, France

[5] Sorbonne Université, CNRS, Institut des Matériaux de Paris-Centre, FR2482, F-75005, Paris France

Benedikt Lassalle-Kaiser benedikt.lassalle@synchrotron-soleil.fr

Christel Laberty-Robert christel.laberty@sorbonne-universite.fr

David Portehault david.portehault@sorbonne-universite.fr

ABSTRACT

Manganese and cobalt perovskite oxides are among the most active precious metal-free electrocatalysts for the oxygen reduction reaction (ORR) and the oxygen evolution reaction (OER), respectively. Herein, we question the role of the cationic composition and charge state in manganite, cobaltite and mixed Mn/Co perovskites on the mechanism of oxygen electrocatalysis for ORR and OER. We synthesize in molten salts a range of perovskite nanoparticles active in ORR (single B-site $(LaMn)_{1-\gamma}O_3$ and $(La_{0.7}Sr_{0.3}Mn)_{1-\gamma}O_3$), in OER (single B-site $La_{0.67}Sr_{0.33}CoO_{3-\delta}$) and in both ORR and OER (mixed B-site $(LaMn_{0.6}Co_{0.4})_{1-\gamma}O_3$). By using *operando* X-ray Absorption Spectroscopy coupled to *ex situ* Electron Energy Loss Spectroscopy, we show that Mn and Co in single B-site perovskites undergo changes in oxidation states at the steady-state during electrocatalysis, while their oxidation states remain unchanged in the mixed Mn/Co perovskite during OER and ORR. We relate these distinct behaviors to modifications of the rate-determining steps of both the OER and ORR electrocatalytic cycles, triggered by an increased covalency of B-O bonds in the mixed perovskites. These results highlight how simple cationic substitutions, accompanied by a control of cationic vacancies, offer a pathway to tune oxygen electrocatalysis.

KEYWORDS:

Electrocatalysis

Oxygen evolution reaction

Oxygen reduction reaction

Perovskites

Nanoparticles

Operando

X-ray absorption spectroscopy

INTRODUCTION

Storing electrical energy is one of the scientific challenges in the transition from fossil fuels to clean and sustainable energy. Electrical energy can be stored into chemical bonds, by electrochemically splitting water to form dihydrogen and dioxygen gases. Most energy losses in low-temperature electrolyzers are due to slow kinetics of the oxygen evolution reaction (OER). Similar losses occur also in fuel cells that consume dihydrogen, due to the poor kinetics of the oxygen reduction reaction (ORR). The need to design active and cost-effective catalysts for OER and/or ORR is therefore providing a strong impetus to the understanding of the mechanisms of oxygen electrocatalysis.[1,2]

ABO_3 perovskite oxides, made of alkaline or rare-earth ions in the A-site and of first row transition metal (TM) cations in the B-site, are efficient OER and/or ORR electrocatalysts in alkaline solution. Some of them exhibit activities rivalling IrO_2 benchmarks.[3] OER and ORR on perovskite oxides can occur through the adsorbate evolution mechanism (AEM),[4–6] where the metal cations are the active sites,[6–9] or through the lattice oxygen mechanism (LOM) involving anionic redox processes on two neighbouring sites.[6,10] In the frame of AEM, the control of the OER/ORR electrocatalytic activity is usually correlated to the impact of the e_g orbitals occupancy and of the covalency of B-O bonds on the kinetics of the rate-determining step.[4–9,11] Likewise, the B-O covalency can also strongly influence the OER kinetics for perovskites operating through LOM.[5]

A number of substituted perovskites have been designed according to these principles, in order to tune the e_g occupancy and the B-O covalency, by substituting the A-site or B-site cations and by incorporating oxygen vacancies.[4–6,11–14] Especially, mixed Mn/Co B-sites lead to OER/ORR bifunctional electrocatalysts.[8] More fundamentally, incorporating Mn on the B site of $LaCoO_3$ reduces the average number of orbital-filling electrons and raises the O 2*p* band closer to the Fermi level, which favours OER kinetics. However, the role of each transition

metal cation in such bimetallic B-site perovskites during OER and ORR electrocatalysis is still to be elucidated. Especially, to what extent the interplay between these cations can change the OER and ORR kinetics? This question is of utmost importance, as it would bring a more predictive approach for the choice of transition metals and of the overall composition of perovskite oxides towards efficient bi-functional electrocatalysts.

We report here the molten salts synthesis of manganese/cobalt perovskite nanoparticles with various compositions. Their high surface-to-volume ratio makes the use of X-ray absorption spectroscopy (XAS) relevant to extract information on the surface states. We then probe their electronic structure with *operando* XAS at the Mn and Co K-edges during OER and ORR electrocatalysis. The analysis of the resting state during electrocatalysis highlights reversible oxidation state changes on the B-site for perovskites built on solely Mn or Co cations. On the other side, mixed manganese/cobalt materials do not show such changes despite similar electrocatalysis. These distinct behaviours point towards different kinetics of oxygen electrocatalysis mechanisms depending on the nature and composition of the B-sites in perovskite electrocatalysts.

RESULTS AND DISCUSSION

Synthesis and characterization of Mn and Co perovskite nanoparticles

The La(Mn,Co)$O_{3\pm\delta}$ perovskite nanocrystals (**LMCO**) were synthesized by adjusting a procedure previously reported for manganite perovskites that relies on molten salts synthesis.[15–17]

Briefly, the synthesis consists in reacting metal nitrate salts in adequate ratios into molten potassium nitrate for 1 h at 600 °C (see details in experimental section). Wavelength-dispersive X-ray fluorescence (WDXRF) indicates Co/Mn ratios of 0.34 and 0.49 at. for **LMCO30** and **LMCO40**, respectively, and a La/(Mn+Co) ratio of 1.1 at. for both samples, which indicates an La excess of ~10% at. compared to the ideal perovskite composition (**Table S-1**). Reference

samples $LaMn^{+3}O_{3\pm\delta}$ (**LMO**, **Figures S-1** and **S-2**), $La_{0.7}Sr_{0.3}MnO_{3\pm\delta}$ (**LSMO**, **Figures S-2** and **S-3**), $La_{0.75}Sr_{0.25}CoO_{3-\delta}$ (**LSCO, Figures S-4** and **S-5**) and $SrMn^{+4}O_{3-\delta}$ (**SMO**) with similar particle size were synthesized by adjusting the procedure described above (see SI). $LaCo^{+3}O_{3-\delta}$ (**LCO**) was obtained through a solid-state reaction (SI).

Transmission electron microscopy (TEM) (**Figure 1a-b**) reveals two populations of objects: nanoparticles with an average diameter of *ca.* 30 nm (**Figure S-6**) and nanowires of diameter *ca.* 40 nm and lengths ranging from 100 to 300 nm (**Figure 1c**). Scanning transmission electron microscopy (STEM) elemental mapping coupled to X-ray energy dispersive (EDX) analysis (**Figure 1c-f**) evidences the homogeneous distribution of La, Mn and Co within the nanoparticles, while only La is detected in the nanowires. X-ray powder diffraction (XRD) reveals that the powder consists in the perovskite phase as major component, with lanthanum trihydroxide as a side-product (**Figure 1g**). The content of $La(OH)_3$ is evaluated to ~10 wt.% according to Rietveld refinement of the powder XRD patterns (**Figure S-7**), in acceptable agreement with WDXRF data (**Table S-1**). Rietveld refinement also indicated no noticeable amounts of crystalline cobalt spinel (**Figure S-7, Table S-1**). The nanowires are therefore attributed to $La(OH)_3$ while the 30 nm nanoparticles correspond to the perovskite phase (**Figure S-8**). Note that $La(OH)_3$ has little activity in ORR[18] and OER,[19] and it is scarce enough to qualitatively assess the electrocatalytic properties of perovskite nanoparticles.

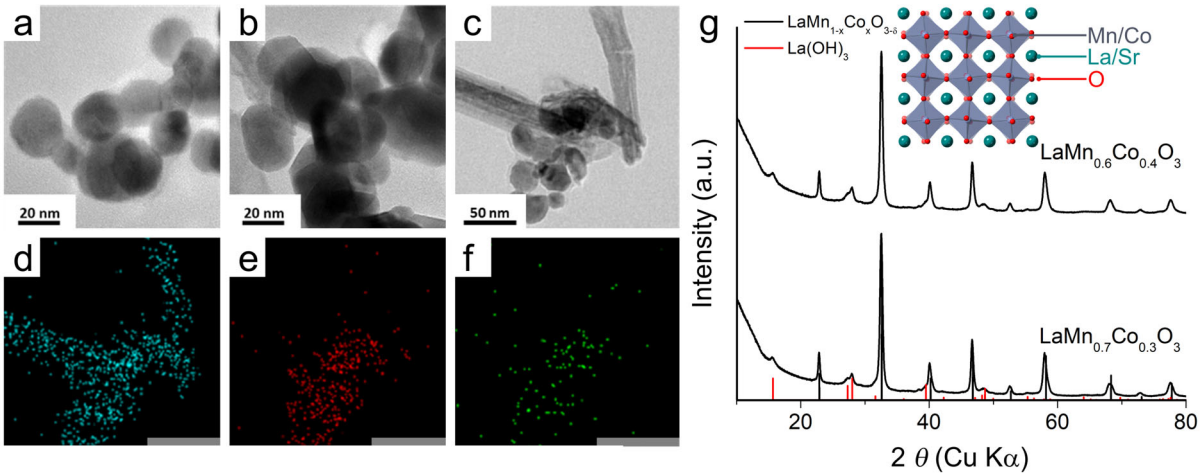

Figure 1. TEM images of (a) **LMCO30** and (b) **LMCO40**, corresponding to $LaMn_{0.7}Co_{0.3}O_{3\pm\delta}$ and $LaMn_{0.6}Co_{0.4}O_{3\pm\delta}$, respectively. (c) STEM and corresponding (d) La, (e) Mn, and (f) Co STEM-EDX maps of the **LMCO30** sample. (g) Powder XRD patterns of the **LMCO30** and **LMCO40** samples. The patterns are indexed versus the $LaMnO_{3\pm\delta}$ structure (black) and $La(OH)_3$ (red) references (see Materials and Methods section).

The oxidation states of Mn and Co were evaluated on the pristine powders by recording the Mn and Co K-edge X-ray absorption near-edge structure (XANES) spectra (**Figure 2a-b**). As A-site La^{3+} is substituted by Sr^{2+} from **LMO** to **LSMO** and **SMO**, a shift of the Mn K-edge toward higher energy is observed (**Figure 2a**), indicating an increase in the average Mn oxidation state, as expected from charge balance. We observe the same trend when substituting Mn by Co from **LMO** to **LMCO30** and **LMCO40**. Linear combination fitting analysis (LCF) of **LSMO**, **LMCO30** and **LMCO40** with **LMO** and **SMO** as references (**Figure S-9**) enables estimating the Mn oxidation state to 3.4±0.1 in **LSMO**, close to the expected value of 3.3 according to the composition evaluated by WDXRF. Following the same analysis procedure, the Mn oxidation state is determined to be 3.6±0.1 and 3.5±0.2 in **LMCO30** and **LMCO40**, respectively. The Co K-edge (**Figure 2b**) of **LSCO** is shifted to higher energy compared to $LaCo^{3+}O_{3-\delta}$ (**LCO**), in agreement with charge balance, thus indicating an average Co oxidation between +3 and +4. A strong shift to lower energies, between Co^{2+} and Co^{3+} K-edges, is observed from **LCO** to **LMCO40** and **LMCO30**. A linear interpolation from the absorption

edge positions of $Co(OH)_2$ (Co^{2+}) and **LCO** (Co^{3+}) yields a Co oxidation state in **LMCO30** and **LMCO40** at *ca.* 2.6. This trend is consistent with the concomitant increase in the average Mn oxidation state (**Figure 2a**) from **LMO** to **LMCO30** and **LMCO40** samples. Such electronic compensation between two coexisting transition metals has been observed in several manganite cobaltite oxides.[20–24]

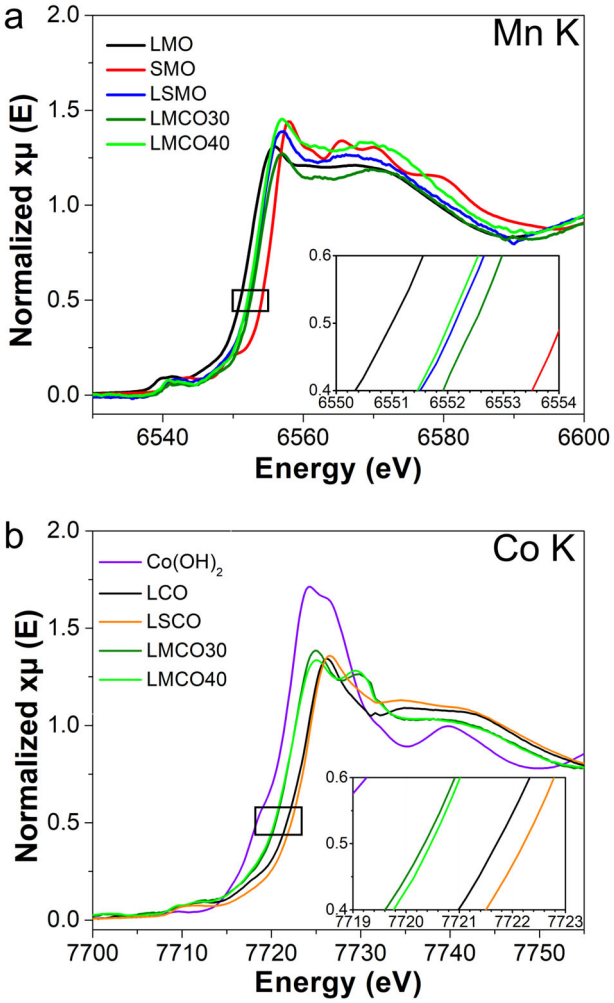

Figure 2. (a) Mn K-edge XANES spectra of powders: **LMO**, **LSMO**, **LMCO30**, **LMCO40**. The references for **SMO** is reported from Celorrio *et al* (CC-BY 4.0).[25] (b) Co-K-edge XANES spectra of powders: **LCO**, **LSCO**, **LMCO30**, **LMCO40** and **$Co(OH)_2$**. The inserts magnify the half-edge jump regions.

Because ORR and OER electrocatalytic properties of perovskites are strongly dependent on the stoichiometry, especially cationic[26] and anionic vacancies,[27] we performed Energy Electron Loss Spectroscopy (EELS) and Energy Dispersive X-ray spectroscopy (EDX) to evaluate the precise composition of single particles. By doing so, we could directly correlate transition metal oxidation states with the cationic composition and then address the question of non-stoichiometry in single particles. As for XANES, manganese and cobalt oxidation states were calculated by interpolating the M-$L_{2,3}$ signal from calibration curves previously recorded (**Figure 3** and **Figure S-10**)[28,29]. The average oxidation states obtained from EELS for Mn and Co and for all assessed materials are consistent with those resulting from the XANES study (**Table S-2)**. By combining XANES, EELS, EDX and WDXRF data, the compositions of **LMCO30** and **LMCO40** are estimated as $(LaMn^{+3.6}_{0.75}Co^{+2.6}_{0.25})_{0.94}O_3$ and $(LaMn^{+3.5}_{0.67}Co^{+2.6}_{0.33})_{0.98}O_3$ respectively.

According to the cationic compositions measured, some samples present an excess of Mn^{3+} or of Mn^{4+} compared to the ideal perovskite stoichiometry. The former must be compensated by oxygen vacancies. The latter must account for cationic vacancies, since manganese and cobalt perovskites cannot accommodate oxygen over-stoichiometry through interstitial sites.[27,30–37] With these considerations in mind, and using the oxidation state values obtained from XANES and EELS, we could evaluate the most likely compositions of the pristine samples (**Table S-3** and **Table 1**). Accordingly, **LSCO** exhibits some anionic vacancies, **LSMO** and **LMCO40** hold cationic vacancies, but the mixed B-site perovskite **LMCO40** stands out with the highest amount of cationic vacancies. Sun *et al.* have suggested that the Co-rich perovskite $LaMn_{0.3}Co_{0.7}O_{3-\delta}$ is prone to oxygen vacancies,[8] like cobalt perovskites. In the Mn-rich sample reported herein, the expected behaviour may be closer to manganese perovskites, which can accommodate oxygen vacancies and cationic vacancies. The

charge compensation mechanism for cationic vacancies observed herein for the mixed Mn/Co B-site perovskite relies only on changes of oxidation states for the B-site cations. This strongly differs from the Co/Fe B-site perovskites, which were suggested to compensate cationic vacancies by oxygen vacancies.[26]

Table 1. Chemical compositions of pristine samples **LMO**, **LSMO**, **LSCO** and **LMCO40** and their evolution during ORR and OER estimated from *operando* XANES.

	Pristine	**OCV**	**ORR**	**OER**
LMO	$LaMnO_3$	$LaMnO_{2.9}$	$LaMnO_{2.7}$	$LaMnO_{2.95}$
LSMO	$(La_{0.7}Sr_{0.3}Mn)_{0.98}O_3$	$(La_{0.7}Sr_{0.3}Mn)_{0.98}O_3$	$La_{0.7}Sr_{0.3}MnO_{2.75}$	-
LSCO	$La_{0.75}Sr_{0.25}CoO_{2.98}$	$La_{0.75}Sr_{0.25}CoO_{2.93}$	$La_{0.75}Sr_{0.25}CoO_{2.83}$	$La_{0.75}Sr_{0.25}CoO_{2.98}$
LMCO40	$(LaMn^{+3.5}{}_{0.67}Co^{+2.8}{}_{0.33})_{0.98}O_3$			

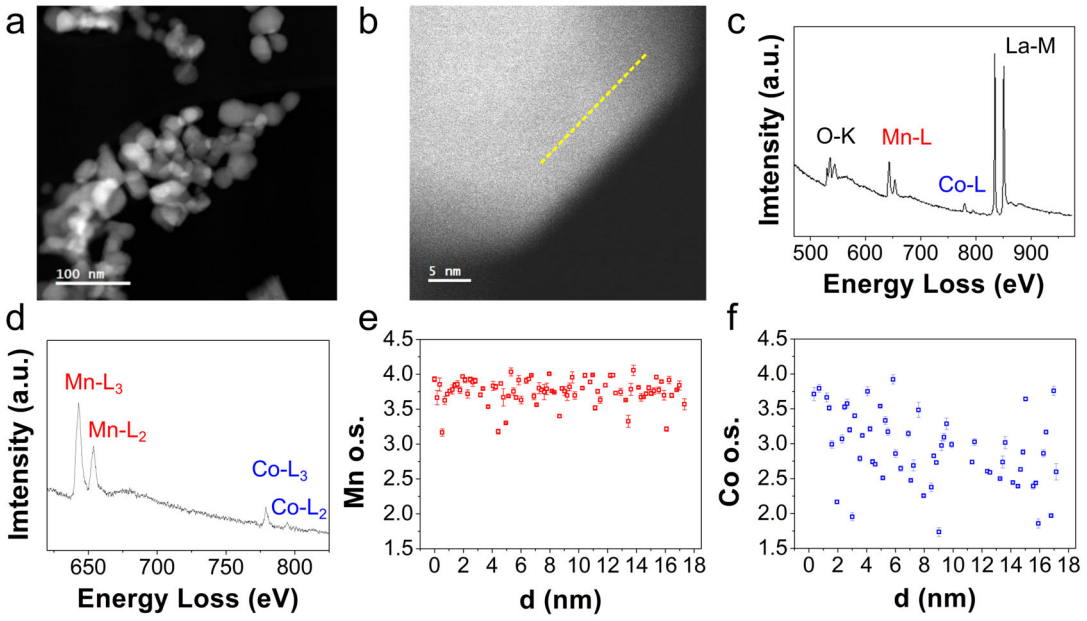

Figure 3. (a) Low and (b) high magnification HAADF-STEM images of **LMCO40**. (c, d) Corresponding EELS sum spectrum, (e) Mn and (f) Co oxidation state measured along the dashed line in (b).

OER and ORR electrocatalytic properties of perovskite nanoparticles

The electrocatalytic properties of the synthesized perovskites have been evaluated for the OER and the ORR in an O_2-saturated 0.1 M KOH electrolyte with a rotating disk 3-electrode setup (**Figure 4** and **S-11**). The currents were normalized *versus* the specific surface area of each electrode material measured by N_2 sorption analysed by the BET method (**Table S-4**). ORR potentials are 0.71, 0.64 and 0.63 V/RHE at 50 $\mu A \cdot cm^{-2}_{oxide}$ for **LMO**, **LMCO30** and **LMCO40**, respectively, in agreement with previous reports on manganite perovskites.[38] OER potentials are *ca.* 1.75 V/RHE at 50 $\mu A \cdot cm^{-2}_{oxide}$ for **LMO**, **LMCO30** and **LMCO40**. The ORR activity of LSMO has been reported elsewhere.[17] The OER activity of **LSCO** (**Figure S-11a**) is in the same order of magnitude as previously reported.[39] While the OER activity is barely modified by the incorporation of cobalt, the ORR activity follows the trend **LMO** > **LMCO40** > **LMCO30** below 0.6 V/RHE. These data suggest that Co substitution does not significantly modify OER properties but slightly impedes the ORR. CVs normalized *versus* the electrochemical surface area (ECSA) show a similar trend for the mixed B-site perovskite (**Figure S-11b**). In order to probe the role of B-site cationic substitution in manganites, we have monitored chemical and structural changes of the nanomaterials during electrocatalysis by using *operando* X-ray absorption spectroscopy (XAS) at the Mn and Co K-edges.

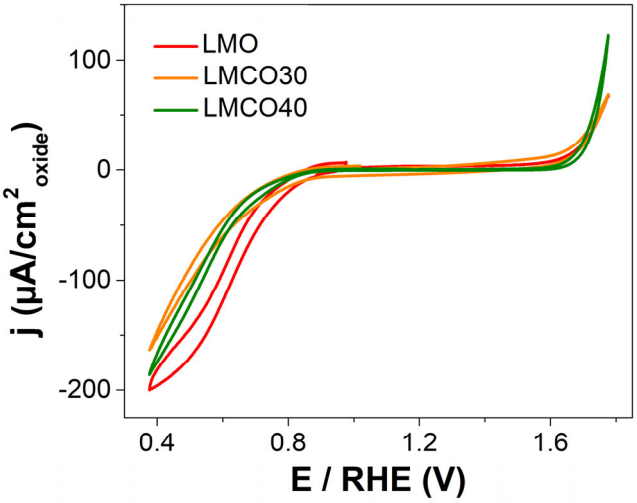

Figure 4. Cyclic voltammograms of **LMO** ($LaMnO_3$), **LMCO30** ($LaMn_{0.7}Co_{0.3}O_{3-\delta}$) and **LMCO40** ($LaMn_{0.67}Co_{0.33}O_{3-\delta}$) samples in an O_2-saturated 0.1 M KOH electrolyte using a rotating disk electrode (1600 rpm) at 10 $mV \cdot s^{-1}$. Electrocatalyst loading: 30 $\mu g \cdot cm^{-2}_{disk}$.

Structural stability of perovskite nanoparticles under electrocatalytic conditions

For all samples studied under electrocatalytic conditions, the intensity of the XAS signal was kept constant (**Figure S-12**) before and after the experiment, which rules out any leaching of transition metal cations. According to TEM (**Figure S-13**), the **LSCO** and **LMCO40** samples recovered from the electrodes after 200 cyclic voltammograms showed no noticeable surface restructuration, whether amorphization or transformation into metal oxyhydroxides, in agreement with our previous observations for **LSMO**.[17] The apparent absence of amorphization is consistent with previous reports[12,40,41] for perovskites of compositions similar to those we studied (LMO, LSMO, LSCO for Sr/(La+Sr) < 0.4 at.). Indeed, surface restructuration is linked to the ability of lattice oxygen anions to undergo exchange with the electrolyte[12,40] and anionic redox reactivity.[12,42] This reactivity is favored when the O *p*-band is close to the Fermi level. In the perovskites considered herein, the O *p*-band is sufficiently far from the Fermi level[12,41] to hinder surface reconstruction during electrocatalysis. We also perform our *operando* investigations at moderate current densities, which again hinders such evolution.[19]

***Operando* X-ray absorption spectroscopy of single metal B-site perovskite electrocatalysts** The results of each *operando* XAS experiment are shown for **LMO** and **LSCO** in **Figures 5a-b** and **5c-d**, respectively (corresponding XANES are displayed in **Figures S-14** and **S-15**). Oxidation states retrieved from these measurements are also summed up in **Table S-5**. Each figure exhibits two panels: the first panel (**Figures 5a** and **c**) shows the electrochemical potential at which the electrode is set, together with the oxidation state of the studied transition metal determined by linear interpolation from the absorption edge energy at half-edge jump of

reference samples as described above. The second panel (**Figures 5b** and **d**) displays difference XANES spectra obtained for each potential step after subtracting the spectra recorded at open circuit voltage (OCV**, Figure S-16**). The differential spectrum of the first OCV is therefore mathematically null.

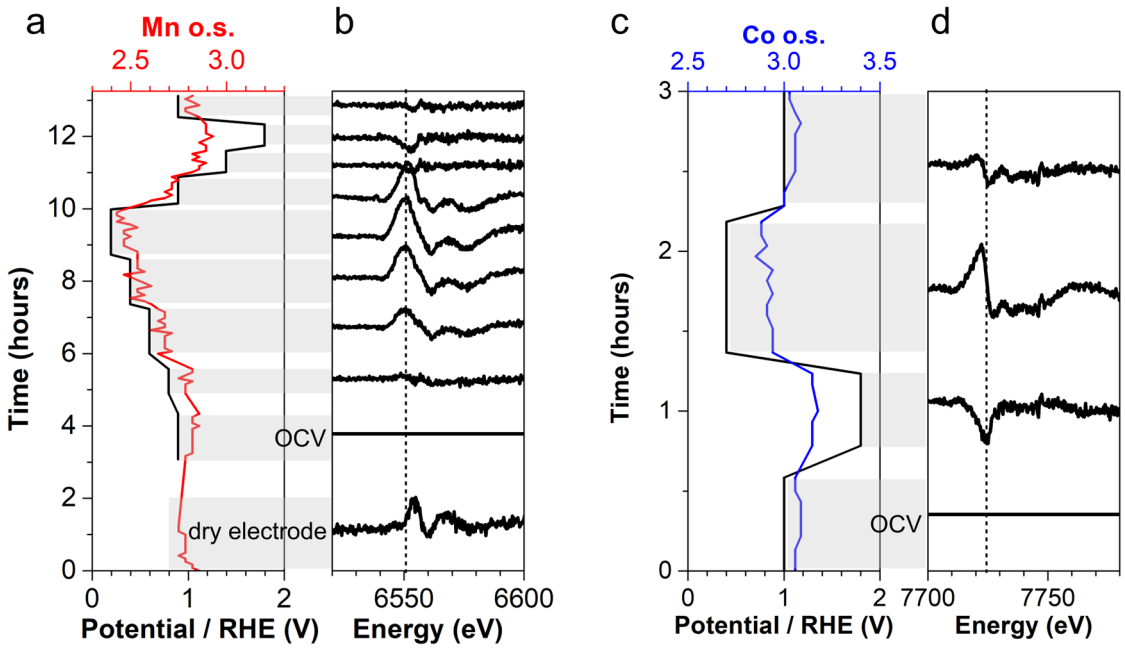

Figure 5. *Operando* XAS study of (a and b) **LMO** and (c and d) **LSCO** during OER and ORR electrocatalysis. (a and c) Time evolution of the oxidation state (red) at different potentials (blue). The period when the potential is not defined (a) corresponds to the dry electrode. The oxidation state is calculated by linear interpolation from the absorption edge positions of pristine **LMO** and **SMO** for Mn, and $Co(OH)_2$ and **LCO** for Co. (b and d): XANES spectra at these potentials, from which the first OCV spectrum is subtracted. The dashed vertical line is the half-edge jump energy of the first OCV spectrum.

A control cyclic voltammogram (CV) (**Figure S-17**) shows that the electrochemical response of **LMO** inside the XAS *operando* cell is comparable to the one recorded with the rotating disk electrode (**Figure 4**) but with lower current, which is ascribed to the absence of convection near the electrode inside the *operando* cell. Bubbles forming at the surface of the working electrode (not shown) further demonstrate the occurrence of OER in the XAS *operando* cell. In order to probe the evolution of the Mn electronic states, we monitored the Mn K-edge over time and in the different electrode states, namely dry state, immersed in the

electrolyte, under ORR and OER conditions (**Figure 5a-b** and **Table S-6**). For **LMO** (**Figure 5a**), the starting Mn oxidation state is below 3, thus below the value of the pristine powder. This suggests reduction during the ink processing and dispersion in ethanol. Then, the oxidation state further decreases overtime in the dry state, down to below 2.8. This phenomenon is attributed to reduction under the beam in the presence of carbon when the material is not cooled down in the electrolyte.[43] Under increasingly reducing conditions (0.6, 0.4 and 0.2 V/RHE), the differential spectra exhibit a rising peak near the K-edge at 6550 eV compared to the reference open circuit voltage (OCV, 0.9 V/RHE) state. This peak indicates a decrease of the edge energy by 1 eV, thus a reduction of manganese under ORR conditions, down to a Mn oxidation state of ca. 2.5 at 0.4 V/RHE, under ORR conditions. The differential peak remains identical after the potential is set back to the OCV. Then, when the electrode is maintained at the OCV, the Mn oxidation state rises up to its original value of 2.9. Therefore, the Mn reduction under ORR conditions is reversible. When increasing the potential from the OCV to 1.4 and then 1.8 V/RHE, the aforementioned differential peak disappears and a small dip appears at 6555 eV, indicating an oxidation of manganese, up to an oxidation state of 3.2 from 1.4 V/RHE and beyond. Finally, the electrode was brought back to the OCV. The flat differential spectrum indicates that the electrode material recovered its initial state and that its oxidation under OER is reversible. The Fourier Transform (FT) of the Extended X-ray Absorption Fine Structure (EXAFS) at the Mn K-edge (**Figure S-18**) shows a first peak at 1.42 Å ascribed to the first Mn-O distance. The magnitude of this peak is correlated to the number of oxygen anions in the Mn coordination sphere. It increases during OER and decreases during ORR, which indicates filling of oxygen vacancies in OER conditions and the creation of oxygen vacancies in ORR conditions.

The evolution of **LSMO** under electrocatalytic conditions (Figures **S-19** to **S-23**, **Tables S-7** and **S-8**) is similar to the one observed for **LMO**, but with higher Mn oxidation

state due to Sr^{2+} doping. When the potential is reduced to 0.2 V/RHE, the Mn average oxidation state decreases from 3.3 to 2.7, indicating the formation of Mn^{2+} under ORR reduction in a perovskite that is initially composed of mixed valence $Mn^{3+/4+}$. A similar observation was made for an electrodeposited δ-$K_xMnO_{2-y}\cdot zH_2O$ electrode.[44]

We then studied the Co electronic state in **LSCO** during ORR and OER by monitoring the cobalt K-edge XANES as a function of time (**Figure 5b and Table S-9**) at different electrochemical potentials. By increasing the potential from OCV (1.0 V/RHE) to OER conditions (1.8 V/RHE), the Co average oxidation state increases from 3.1 to 3.2. When decreasing the potential down to ORR conditions (0.4 V/RHE), the differential spectrum displays an intense peak at the Co K-edge at 7720 eV, a small peak at 7730 eV and a large bump at 7770 eV, with a decrease of the Co oxidation state from 3.2 to 2.9.[12] Co is also bound to less oxygen anions during ORR than during OER according to the FT-EXAFS (**Figure S-24**), in agreement with the evolution of the Mn coordination described above for **LMO** and **LSMO**. When the electrode is brought back to the OCV, the Co average oxidation state recovers its initial value of 3.1 at the OCV. The differential spectrum also shows a decrease in the intensity of the peak at 7720 eV, but a remaining peak at 7730 eV. Therefore, although changes in the oxidation state of Co during OER and ORR appear reversible, some structural changes under ORR conditions remain after operation. Overall, cobalt in **LSCO** follows the same trend as manganese in **LMO** and **LSMO**: the transition metal oxidizes during OER and reduces during ORR. These changes are quasi-reversible, since bringing back the electrode materials from ORR conditions to the OCV is not sufficient to fully recover the initial state within 1 h.

***Operando* X-ray absorption spectroscopy of mixed metal B-site perovskite electrocatalysts**

We then assessed the evolution during electrocatalysis of the redox states for the mixed Mn and Co perovskite with the largest Co content, **LMCO40** (**Figures S-25** to **S-30** and **Table S-10**), as it exhibits higher activity than LMCO30. Manganese and cobalt K-edge spectra were recorded successively at each potential step. XANES spectra were collected and averaged for 20 and 40 min at the Mn (**Figure 6a-b**) and Co (**Figure 6c-d**) K-edges, respectively, in order to reach a sufficient signal-to-noise ratio for each metal despite their different contents. The Mn and Co oxidation states measured *operando* are *ca.* +3.4 and +2.6, respectively. They are higher and lower, respectively, than those of their single metal counterparts (see **Figure 7** and **Table S-5).** For each element, no modification in the overall shape of the spectra nor in the edge energies is observed after 1 hour at a constant potential, whether under ORR or OER conditions. Contrary to single B-site perovskite detailed above, no significant change of the Mn and Co coordination spheres is observed by EXAFS from OER to ORR conditions (**Figures S-29** and **S-30**). This indicates that no change of oxidation state or of local structure occur for both the manganese and cobalt cations. This behaviour is in sharp contrast with the clear changes of oxidation states observed for the single B-site perovskites **LMO**, **LSMO** and **LSCO**.

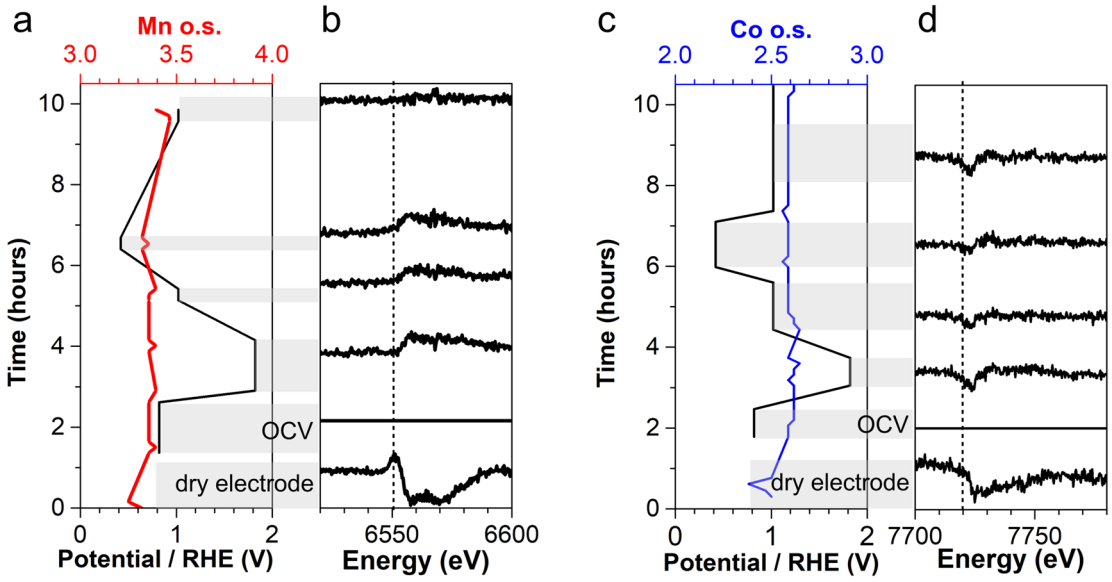

Figure 6. Evolution of XANES spectra and oxidation state of (a and b) Mn and (c and d) Co of **LMCO40** from *operando* XAS during OER/ORR electrocatalysis. (a and c) Time

evolution of the oxidation state at different potentials. The period when the potential is not defined corresponds to the dry electrode. The oxidation state is calculated by linear interpolation from the absorption edge positions of pristine **LMO** and **SMO** for Mn, and $Co(OH)_2$ and **LCO** for Co. (b and d) XANES spectra of **LMCO40** at these potentials, from which the first OCV spectrum (0.9 V/RHE) is subtracted. The dashed vertical line is the half-edge jump energy of the first OCV spectrum.

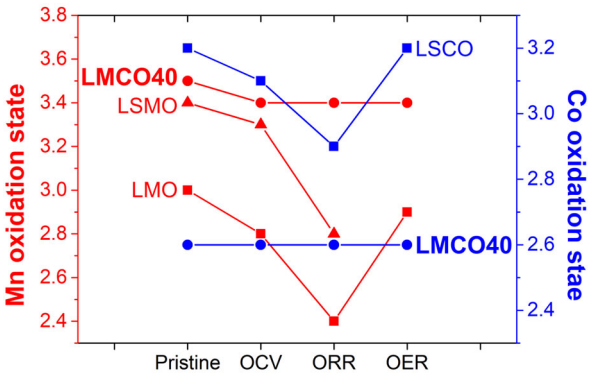

Figure 7. *Operando* evolution of the manganese (red) and cobalt (blue) oxidation states in perovskites under ORR and OER conditions.

We evaluated the evolution of the anionic compositions of the samples probed *operando* from the average Mn and Co oxidation states, with the assumptions made above for the pristine samples (**Table 1**). The compositions are steady when the electrodes are immersed in the basic electrolyte (OCV conditions). During electrocatalysis, some samples exhibit significant composition deviations from the pristine states, but they are maintained in the stable stoichiometry range of manganese and cobalt perovskites,[27,30–37] thus supporting the stability of these materials under ORR and OER conditions. **LMO**, **LSMO** and **LSCO** are reduced under ORR conditions, which is compensated by the creation of oxygen vacancies. These transformations are reversible and the materials recover compositions close to the initial ones under oxidative OER conditions (**LSMO** is inactive in OER and has not been evaluated in these conditions). The mixed B-site perovskite **LMCO40** stands out from the other samples, as we do not observe any significant change in the composition during electrocatalysis, as mentioned above for the Mn and Co oxidation states.

The mixed B-site perovskite exhibits a deviation of Mn and Co oxidation states compared to single B-site perovskites. Mn^{2+} forms *operando* under ORR conditions in **LMO** and **LSMO** (average oxidation states below +3, **Figure 7** and **Table S-5**). Likewise, Co^{4+} is detected *operando* under OER conditions (average oxidation states above +3, **Figure 7**). On the opposite, Mn^{2+} and Co^{4+} are not observed in **LMCO40**, which contains under all conditions mixed valences $Mn^{3+/4+}$ and $Co^{2+/3+}$. Hence, an electron transfer occurs from Mn^{2+} to Co^{4+} in the mixed perovskite. Although Mn and Co species are usually considered as active sites of ORR and OER electrocatalysts,[4,5] respectively, one may notice that Mn^{3+} and Mn^{4+} encountered in **LMCO40** are proposed to be intermediates in the water oxidation reaction for several OER-active manganese oxides[45,46] as well as in the Oxygen Evolving Complex of Photosystem II.[47] Conversely, Co^{2+} present in **LMCO40** has been proposed as an ORR active species.[48] Therefore, Mn and Co cations may act together as active sites in **LMCO40** for both ORR and OER.

The behaviour we observe during electrocatalysis can be discussed in the mechanistic frame of OER/ORR on perovskites.[13,14] **LSCO** (Sr/(La+Sr) < 0.4 at.) has been shown to perform alkaline OER through the AEM.[6,41,49] For perovskites that do not undergo surface amorphization, OER (and ORR) following the AEM are usually considered to occur through four coupled proton-electron transfers.[13,14] In this mechanism, the rate-determining step (RDS) is often the formation of a $B^{m+}(OOH)$ intermediate from $B^{(m+1)+}(O^{2-})$ [14] (step 2 on **Figure 8a**) or its deprotonation to form a $B^{(m+1)+}(O_2^{2-})$ species (step 3 on **Figure 8a**). *Operando* XAS shows that the OER resting state for **LSCO** corresponds to an accumulation of B species with increased oxidation state. This might indicate either that the formation of the O-O bond (step 2) is the RDS, or that it is a pre-equilibrium exists between $B^{(m+1)+}(O^{2-})$ and $B^{m+}(OOH)$, displaced towards $B^{m+1}(O^{2-})$. In this case, step 3 would then be the RDS. Although the latter case has been proposed for cobalt oxyhydroxide operating through the LOM,[42] to our

knowledge there has been no evidence of a pre-equilibrium for perovskites operating through the AEM mechanism.[6,41,49] Considering the O-O bond formation (step 2) as the RDS is also consistent with most mechanistic proposals.[13,14] A similar reasoning can be made for **LMO** during OER.

Under ORR conditions, the RDS is expected to be the protonation and reduction of $B^{(m+1)+}(O^{2-})$ species (step IV **Figure 8b**), or the binding of O_2 and release of OH^- concomitant with an increase of the B oxidation state (step I **Figure 8b**).[14] *Operando* XAS data collected during ORR on all single B-site perovskites studied herein (**LMO**, **LSMO** and **LSCO**) show reduced B-site cations in the resting state as compared to their initial states. Although we cannot exclude the occurrence of a pre-equilibrium, we note that this possibility has not been proposed in previous mechanistic ORR proposals,[4,11,14] and that the displacement of a surface hydroxide group by O_2 (step I **Figure 8b**) is the most common RDS for ORR on perovskite oxides,[4] in agreement with our data. For both OER and ORR, our data for single B-site perovskites are then consistent with RDSs corresponding to the reaction of $B(O^{2-})$ or $B(OH^-)$ moieties to form peroxo species.

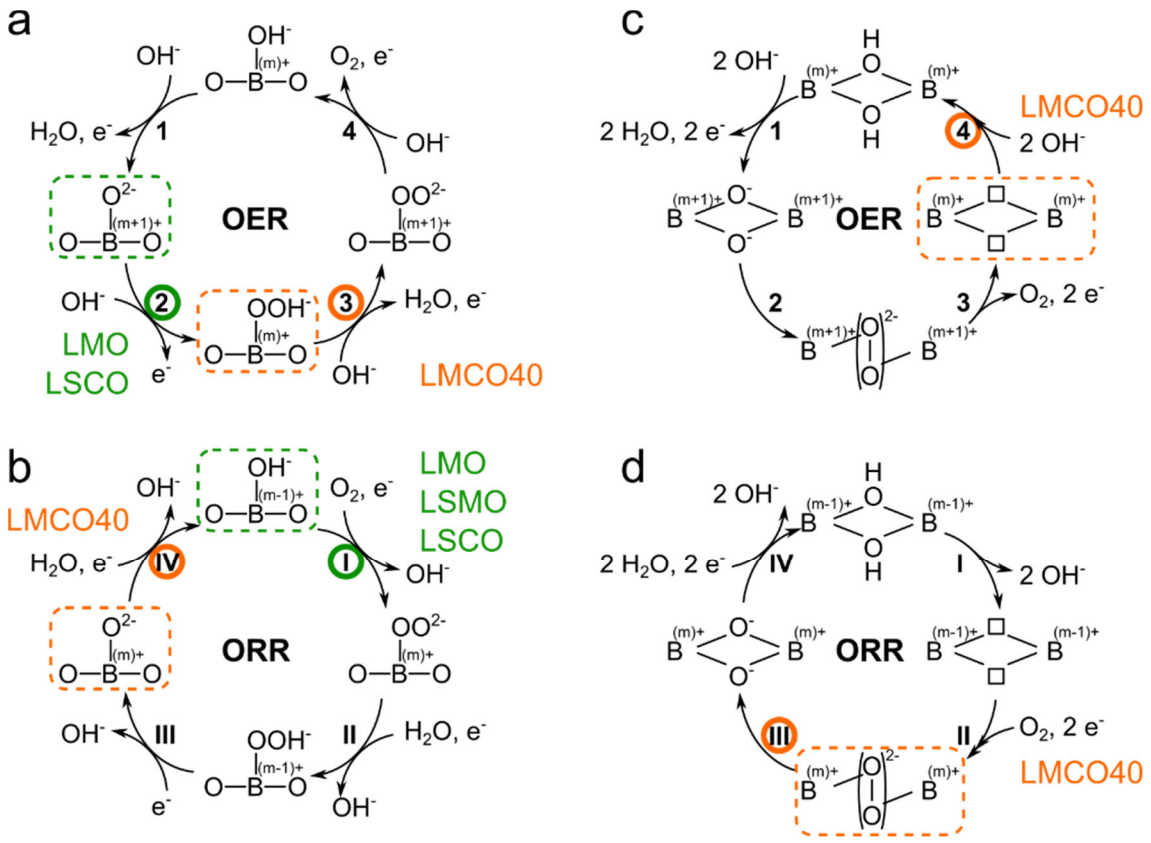

Figure 8. (a, b) Classical four-steps AEM mechanism of proton-coupled electron transfer for (a) the OER and (b) the ORR. (c, d) Possible LOM mechanism based on an anionic redox process for (c) the OER and (d) the ORR. Green circles in (a) and (b) highlight the rate-determining steps (RDS) for single B-site perovskites. Orange circles show the plausible RDS for the mixed B-site perovskite **LCMO40**. Dashed boxes highlight the major species at the steady state detected by *operando* XAS.

The mixed B-site perovskite **LMCO40** exhibits a behaviour opposite to single B-site compounds, as the oxidation state of the B-site cations is unchanged in the resting state. To understand this drastic difference, we further examine the impact of the *ex situ* and *operando* chemical compositions of the perovskites on the nature of the B-O bonds. The covalency of the B-O bond in manganese perovskites is increased by substituting the B-site cation with a more electronegative metal, such as cobalt, and by increasing the manganese oxidation state.[6,11,14] The B-O covalency is also enhanced by incorporating cationic vacancies.[6] We note that under OER operating conditions, **LMCO40** exhibits the highest Mn oxidation state and the highest amount of cationic vacancies (**Table 1**) among the studied compounds. Hence, the electronic state and composition of the mixed Mn/Co perovskite enhance the B-O covalency. This increase

of covalency has been shown[4–6] to increase the rate of both OER and ORR, especially the steps involved in the formation of peroxo species, which we identified above as plausible OER/ORR RDSs for the single B-site perovskites. We can then assume that due to increased covalency, these steps could be fast enough on the mixed B-site perovskite to trigger a change in the RDSs.

Increasing the covalency of the B-O bond facilitates the deprotonation of the hydroxo or peroxo ligands, which makes the existence of pre-equilibra for steps 1 and 3 (**Figure 8a**) of the OER AEM cycle even less likely than for the single B-site perovskites.

Again with the assumption that there is no pre-equilibrium for OER on perovskite surfaces operating through the AEM mechanism,[6,41,49] the identification by XAS of unchanged oxidation state suggests that steps 1 or 3 (**Figure 8a**) would be the OER RDS. With a similar reasoning, the opposite reactions (steps II and IV, **Figure 8b**) then become possible ORR RDSs. Given that the same steps are not RDS for OER and ORR, either hydroxyl deprotonation and protonation of the peroxo group are the OER and ORR RDSs, respectively, or OOH deprotonation (step 3, **Figure 8a**) and hydroxyl regeneration (step IV, **Figure 8b**) are the OER and ORR RDSs, respectively. The second hypothesis corresponds to a more frequent case for perovskites (**Figure 8a-b**).[5] It is also consistent with the lower impact of the increased B-O covalency on the deprotonation of OOH ligands as compared to OH ligands. Hence, for the mixed perovskite, we identify the OOH deprotonation (step 3) and the hydroxyl regeneration (step IV) as the most plausible RDSs for OER and ORR, respectively.

Noteworthy, an increase of the B-O covalency can also trigger a switch of the ORR/OER mechanism, from cation-based AEM (Fi**gure 8a-b**) to anion-based LOM (**Figure 8c-d**).[6,11] Indeed, while AEM occurs when the oxygen *p* band is lower in energy than the metal *d* band, favoring the metal cation as adsorption center, LOM can occur when the oxygen *p* band comes closer to or overlaps with the metal *d* band. In this energetic configuration, some O 2*p* electrons are transferred to the metal *d* band, so that the redox

processes occur on the anionic sublattice.[6,11,14] According to the absence of change of the oxidation states of B cations at the OER/ORR steady-states, the LOM RDSs for the mixed B-site perovskite would be hydroxyl deprotonation (step 1, **Figure 8c**) or hydroxyl uptake (step 4, **Figure 8c**) for OER and O-O splitting (step III, **Figure 8d**) or hydroxyl regeneration (step IV, opposite to step 1 in OER, **Figure 8d**) for ORR. As the same step would not be RDS for the two opposite reactions OER and ORR, then the LOM RDSs would be probably hydroxyl uptake for OER (step 4, **Figure 8c**) and O-O splitting for ORR (step III, **Figure 8d**). This discussion relates to the catalytic cycle commonly proposed for LOM on perovskites where no pre-equilibrium is considered,[6,14] but mechanisms involving a pre-equilibrium have been unambiguously identified for OER involving lattice oxygen on cobalt oxyhydroxides.[42,50] Accordingly, that more complex catalytic cycles should probably be considered as well for perovskites, which is out of the scope of this study. While the present data do not allow distinguishing between AEM and LOM, we note that LOM is usually observed for materials exhibiting significant amounts of oxygen vacancies, which are not observed for the mixed B-site perovskite examined here. However, LOM usually occurs together with AEM at a varying extent.[14] Hence, we do not discard the occurrence of both mechanisms in the mixed B-site perovskite, although our data indicate changes in the rate-determining steps between single and mixed B-site perovskites during OER and ORR.

CONCLUSION

By synthesizing single and mixed B-site perovskite nanoparticles, we have designed bifunctional electrocatalysts for alkaline water oxidation and oxygen reduction. We have combined advanced electron energy loss spectroscopy coupled to transmission electron microscopy with *ex situ* and *operando* X-ray absorption spectroscopy (XAS) in order to provide detailed insights into the perovskite composition and the evolution of the electronic states of

manganese and cobalt cations in the perovskite B-site. Probing the resting state during electrocatalysis by *operando* XAS enabled to propose rate-determining steps for water oxidation and oxygen reduction reactions. For single B-site manganite and cobaltite perovskites, these steps agree with the classical coupled proton-electron transfer mechanism where the B-site cations are the active sites. On the opposite, the absence of change of oxidation state in the resting state for a mixed Mn/Co B-site perovskite indicates a modification of the rate-determining step. We relate this behaviour to an increase of the B-O covalency through the formation of the cationic vacancies upon partial cationic substitution. Therefore, our work shows how the interplay between cationic substitutions, electron transfer between transition metals and the formation of cationic vacancies, can be adjusted to modify the kinetics of oxygen electrocatalysis.

MATERIALS AND METHODS

The synthesis of strontium doped lanthanum manganite (LSMO) was performed according to a procedure reported previously.[15]

Synthesis of manganite cobaltite LMCO40

The manganite perovskites were synthesized from the nitrate precursors $La(NO_3)_3{\cdot}6H_2O$ (Sigma-Aldrich, > 99 %, 8.1 mmol), $Mn(NO_3)_2{\cdot}4H_2O$ (Aldrich, 98 %, 5.6 mmol), $Co(NO_3)_2{\cdot}6H_2O$ (Alfa Aesar, > 98 %, 2.7 mmol) and KNO_3 (Sigma-Aldrich, > 99%, 80 mmol). The powder mixtures were coarsely grinded with a few drops of ethanol in a ball miller (20 Hz, 2 min) and dried in a vacuum oven (60 °C) for at least 24 hours. For each sample, 2.5 g of the corresponding powder was put into an alumina crucible and placed for one hour in a muffle furnace under air and preheated at 600 °C. The crucible was then removed from the hot oven

and cooled down at room temperature, under air. The recovered black solid was dispersed in deionized water (c.a. 60 mL). The dispersion was centrifuged (20 000 rpm for 20 min) then the transparent supernatant was removed. The remaining black solid was redispersed in deionized water and washed by ten centrifugation-redispersion cycles until the supernatant conductance reached a value of 20 µS cm^{-1}. The powders were finally dried under vacuum at 60 °C overnight.

Synthesis of cobaltite LSCO

The cobaltite perovskites were synthesized from the nitrate precursors $La(NO_3)_3 \cdot 6H_2O$ (Sigma-Aldrich, > 99 %, 4.7 mmol), $Sr(NO_3)_2$ (Aldrich, 99 %, 2.4 mmol), $Co(NO_3)_2 \cdot 6H_2O$ (Alfa Aesar, > 98 %, 6.9 mmol) and $NaNO_2$ (Sigma-Aldrich, > 99%, 471 mmol). The solid mixture was coarsely grinded with a ball miller (20 Hz, 2 min) and dried in a vacuum oven (60 °C) for 3 hours and grinded again with a mortar. It was then dried again in the vacuum oven for more than 24 hours to avoid extra-hydration of precursors. 2.5 g of the powder was put into an alumina crucible and placed in a muffle furnace under air and preheated at 700 °C for one hour. The crucible was then removed from the oven and cooled down at room temperature. The recovered black solid was dissolved in deionized water (c.a. 100 mL). The dispersion was centrifuged (20 000 rpm) then the transparent supernatant was removed. The remaining black powder was redispersed in deionized water, washed and dried as the manganese perovskites described above.

Synthesis of cobaltite LCO

The cobaltite perovskite LCO was obtained by solid state synthesis. La_2O_3 (6 mmol) and Co_3O_4 (4.1 mmol) previously dried were grounded and heated at 1100 C for 24 h.

X-ray diffraction

Powder X-ray diffraction (XRD) was performed on a Bruker D8 advance diffractometer equipped with a Cu K_α source ($K_{\alpha1}$= 1.5406 Å, $K_{\alpha2}$= 1.5443 Å) in reflection mode, with an accelerating voltage of 40 kV and a current of 40 mA. The PDF reference cards for $La_{0.67}Sr_{0.33}MnO_3$, $La_{0.67}Sr_{0.33}CoO_3$ and $La(OH)_3$ were 04-014-4312, 04-014-1579 and 04-005-8587 respectively. The ICSD reference card for $LaMnO_3$ is 1542145.

Overall compositions

The atomic composition was measured by wavelength-dispersive X-ray fluorescence (WDXRF) on pelletized powders with a Bruker S8 Tiger spectrometer equipped with a Rh tube.

Transmission electron microscopy

Transmission electron microscopy (TEM) was performed on a FEI Spirit 2 apparatus operating at 120 kV. Qualitative STEM-EDX elemental mapping was performed on a JEOL JEM 2100 Plus LaB_6 working at an accelerating voltage of 200 kV. The powders were deposited on carbon-coated copper grids by drop casting an ethanolic suspension of the particles.

Scanning transmission electron microscopy-Energy Electron Loss Spectroscopy (EELS) was performed in a probe spherical aberration corrected microscope JEOL JSM-ARM200F (Cold Emission Gun) operating at 120 kV. High angle-annular dark field (HAADF) images were acquired at 68-280 mrad inner and outer collection semi-angles. EELS experiments were acquired using a GIF-QuantumER with a collection and covergence semiangle of 18 mrad and 20.3 mrad, respectively. Dual EELS function of the GIF-QuantumER spectrometer was used to record simultaneously zero-loss peak and core region in order to minimize the uncertainty on the energy shift. EEL spectrums were acquired by using spectrum line mode, with 0.25 and 0.1 eV energy dispersion per channel, an acquisition time of 0.5 s over

an average total number of 100 to 150 points per particle, in a total of 20 particles per composition, and pixel size of 2 Å. Principal component analysis was performed on EELS data set to de-noise the spectra by using the MSA (multivariate statistical analysis) plugins for the GatanDMS analysis toolbox[51].

Transition metal oxidation states have been analyzed from electron loss near energy edge structure (ELNES) of Mn $L_{2,3}$ and Co-$L_{2,3}$ edges. Numerical values were estimated by M-$L_{2,3}$ interpolation in the fitting curves reported by M. Varela et al.[28] and Z. L. Wang et al.[29], respectively and error bars by repeating $L_{2,3}$ calculation, modifying integrate window position ± 1 pixel.

Quantitative EDX was performed in a JEOL-JEM GRAND ARM 300cF microscope (Cold Emission Gun) equipped with SDD CENTURIO spectrometer, operated at 120 kV. The experimental error of this technique is in the order of 1 at.%.

Ex situ electrochemical measurements

A composite ink was prepared from the electrocatalyst (10 mg), activated acetylene black (Alfa Aesar, 99.9 %, 10 mg) and absolute ethanol (VWR, 10 mL). It was sonicated for 2 hours and Nafion dispersed in ethanol (Sigma Aldrich, 5 % dispersion, 435 µL) was added. The suspension was sonicated again for 30 min. The electrochemical experiments were carried out less than 12 hours after starting the preparation of the ink.

The rotating disk electrode (RDE, Bio-logic) glassy carbon substrate (ø = 3 mm) was previously polished consecutively on a 1 µm paper (Buehler TexMet C, 5 min) and a 0.05 µm paper (Buehler ChemoMet, 5 min). 2 µL of the ink was then dropped on the substrate. The deposit was dried for 30 min in air. A few microliter of electrolyte was then dropped on the substrate to wet the electrode. After 30 min, the substrate was connected to the RDE. The 0.1 M KOH (Alfa Aesar, 85 %) electrolyte was prepared the day of the electrochemical experiments.

The electrochemical measurements were carried out in a plastic beaker to prevent any glass dissolution from a glass beaker in the alkaline electrolyte. The electrolyte was saturated with dioxygen by bubbling for 30 min before the beginning of the experiment and all along the measurement during both OER and ORR experiments. The reference electrode was a saturated Ag/AgCl electrode ($E^0 = 0.197$ V/SHE). The counter electrode was a platinum wire separated from the electrolyte with a frit. The working electrode was on RDE (Bio-logic) equipped with nanoparticle ink-coated glassy carbon substrate tip. The cyclic voltammograms were recorded at a sweep rate of 10 $mV \cdot s^{-1}$ over 5 cycles with the RDE rotating at 1600 rpm. For the OER/ORR experiments (**LMO**, **LSCO** and **LMCO** samples), the cyclic voltammograms were recorded from the OCV to 1.8 V/RHE, then 0.4 V/RHE, then back to OCV.

XAS setup

XAS spectra were recorded on the SAMBA beamline at the SOLEIL synchrotron (Si(220) monochromator, $\Delta E/E = 6 \times 10^{-5}$, Canberra Ge 35-pixel fluorescence detector) and on the B18 beamline at the DIAMOND synchrotron (Si(111) monochromator, $\Delta E/E = 1.4 \times 10^{-4}$, 4 elements Si drift fluorescence detector). The Co K-edge spectra were collected between 7510 and 8560 eV in a step mode with a scan rate of 3.5 $eV.s^{-1}$ and an integration time of 0.07 s per point for a recording time between 6 and 7 min. The Mn K-edge spectra were collected between 6340 and 7390 eV in a step mode with a scan rate of 3.5 $eV \cdot s^{-1}$ with an integration time of 0.07 s per point for a recording time of 5 min per scan. The XAS spectra were recorded in fluorescence mode and normalized by a I_0 measured before the sample. The *operando* electrochemical cell was similar to the one described by Lassalle *et al.*[52] The reference was a saturated calomel electrode (0.244 V/NHE). The counter electrode was a platinum wire in a frit. The working electrode was a glassy carbon plate covered with an electrocatalyst ink (ca. 20 $\mu L \cdot cm^{-2}$ and 20 µg of catalyst per cm^{-2}, geometric active surface of ca. 1 cm^{-2}). The plate was

glued on a hole on the side of the cell delimiting the geometric active surface so that one side was in contact with the electrolyte, and the other side was directly exposed to the incident X-rays. In this configuration, X-rays are only absorbed by the components of the working electrode, namely the glassy carbon plate whose thickness is 60 µm and the electrocatalyst ink. The vertical position of the working electrode allows oxygen bubbles that are formed during OER to escape to the surface of the aqueous electrolyte, and thus refresh the species near the electrocatalysts. The cell is large enough to add an oxygen bubbling inlet for ORR/OER experiments.

Operando XAS measurements

All *operando* XAS experiments were preceded by a control cyclic voltammogram. The control CVs and the potential steps are summarized in the supplementary information. For the study of **LMCO40**, more scans were recorded at a given potential to account for the lower amount of Co with respect to Mn.

SUPPORTING INFORMATION. Compositional, structural and morphological characterization of the different samples (Tables S-1 to S-4, Figures S-1 to S-10), electrochemical characterization performed *ex situ* (Figure S-10) and in situ coupled to post-OER analysis (Tables S-5 to S-10, Figures S-12 to S-30).

ACKOWLEDGEMENTS

The authors acknowledge Patricia Beaunier from the Institut des Materiaux de Paris Centre for STEM. This work was supported by the French national agency for research (ANR) under the project InSiChem ANR-16-CE05-0011. This project has received funding from the European Research Council (ERC) Consolidator Grant GENESIS under the European Union's Horizon 2020 research and innovation programme (grant agreement n° 864850). The experiments at the

SAMBA beamline at Synchrotron SOLEIL have been funded by SOLEIL under the User Proposal 20181146. The experiments at the B18 beamline a Diamond Light Source have been funded by Diamond under the proposal SP21747-1. J.M.G.C. and M.L.R.G. acknowledge financial support by the Spanish Ministry of Science and Innovation through Research Project PID 2020-113753RB-100. The National Centre for Electron Microscopy (ELECMI National Singular Scientific Facility) is also acknowledged for provision of access to corrected aberration microscopy facilities.

REFERENCES

(1) Lu, Y.-C.; Gallant, B. M.; Kwabi, D. G.; Harding, J. R.; Mitchell, R. R.; Whittingham, M. S.; Shao-Horn, Y. Lithium–Oxygen Batteries: Bridging Mechanistic Understanding and Battery Performance. *Energy Environ. Sci.* **2013**, *6* (3), 750. https://doi.org/10.1039/c3ee23966g.

(2) de Miranda, P. E. V. Hydrogen Energy. In *Science and Engineering of Hydrogen-Based Energy Technologies*; Elsevier, 2019; pp 1–38. https://doi.org/10.1016/B978-0-12-814251-6.00001-0.

(3) Lee, Y.; Suntivich, J.; May, K. J.; Perry, E. E.; Shao-Horn, Y. Synthesis and Activities of Rutile IrO_2 and RuO_2 Nanoparticles for Oxygen Evolution in Acid and Alkaline Solutions. *J. Phys. Chem. Lett.* **2012**, *3* (3), 399–404. https://doi.org/10.1021/jz2016507.

(4) Suntivich, J.; Gasteiger, H. A.; Yabuuchi, N.; Nakanishi, H.; Goodenough, J. B.; Shao-Horn, Y. Design Principles for Oxygen-Reduction Activity on Perovskite Oxide Catalysts for Fuel Cells and Metal-Air Batteries. *Nat. Chem.* **2011**, *3* (7), 546–550. https://doi.org/10.1038/nchem.1069.

(5) Suntivich, J.; May, K. J.; Gasteiger, H. a; Goodenough, J. B.; Shao-Horn, Y. A Perovskite Oxide Optimized for Oxygen Evolution Catalysis from Molecular Orbital Principles. *Science* **2011**, *334* (6061), 1383–1385. https://doi.org/10.1126/science.1212858.

(6) Song, J.; Wei, C.; Huang, Z. F.; Liu, C.; Zeng, L.; Wang, X.; Xu, Z. J. A Review on Fundamentals for Designing Oxygen Evolution Electrocatalysts. *Chem. Soc. Rev.* **2020**, *49* (7), 2196–2214. https://doi.org/10.1039/C9CS00607A.

(7) Liu, X.; Gong, H.; Wang, T.; Guo, H.; Song, L.; Xia, W.; Gao, B.; Jiang, Z.; Feng, L.; He, J. Cobalt-Doped Perovskite-Type Oxide $LaMnO_3$ as Bifunctional Oxygen

Catalysts for Hybrid Lithium–Oxygen Batteries. *Chem. Asian J.* **2018**, *13* (5), 528–535. https://doi.org/10.1002/ASIA.201701561.

(8) Sun, J.; Du, L.; Sun, B.; Han, G.; Ma, Y.; Wang, J.; Huo, H.; Du, C.; Yin, G. Bifunctional $LaMn_{0.3}Co_{0.7}O_3$ Perovskite Oxide Catalyst for Oxygen Reduction and Evolution Reactions: The Optimized Eg Electronic Structures by Manganese Dopant. *ACS Appl. Mater. Interfaces* **2020**, *12* (22), 24717–24725.

(9) Yoo, J. S.; Rong, X.; Liu, Y.; Kolpak, A. M. Role of Lattice Oxygen Participation in Understanding Trends in the Oxygen Evolution Reaction on Perovskites. *ACS Catal.* **2018**, *8* (5), 4628–4636. https://doi.org/10.1021/ACSCATAL.8B00612.

(10) Wang, L.; Li, H.; Liu, J.; Lang, X.; Wang, W. Labile Oxygen Participant Adsorbate Evolving Mechanism to Enhance Oxygen Reduction in $SmMn_2O_5$ with Double-Coordinated Crystal Fields. *J. Mater. Chem. A.* **2021**, *9* (1), 380–389. https://doi.org/10.1039/d0ta09537k.

(11) Hwang, J.; Rao, R. R.; Giordano, L.; Katayama, Y.; Yu, Y.; Shao-Horn, Y. Perovskites in Catalysis and Electrocatalysis. *Science* **2017**, *358*, 751–756.

(12) Grimaud, A.; May, K. J.; Carlton, C. E.; Lee, Y.-L.; Risch, M.; Hong, W. T.; Zhou, J.; Shao-Horn, Y. Double Perovskites as a Family of Highly Active Catalysts for Oxygen Evolution in Alkaline Solution. *Nat. Commun.* **2013**, *4*, 2439. https://doi.org/10.1038/ncomms3439.

(13) Grimaud, A.; Diaz-Morales, O.; Han, B.; Hong, W. T.; Lee, Y. L.; Giordano, L.; Stoerzinger, K. A.; Koper, M. T. M.; Shao-Horn, Y. Activating Lattice Oxygen Redox Reactions in Metal Oxides to Catalyse Oxygen Evolution. *Nat. Chem.* **2017**, *9* (5), 457–465. https://doi.org/10.1038/nchem.2695.

(14) Grimaud, A.; Hong, W. T.; Shao-Horn, Y.; Tarascon, J. M. Anionic Redox Processes for Electrochemical Devices. *Nat. Mater.* **2016**, 121–126. https://doi.org/10.1038/nmat4551.

(15) Thi N'Goc, H. Le; Mouafo, L. D. N.; Etrillard, C.; Torres-Pardo, A.; Dayen, J.-F.; Rano, S.; Rousse, G.; Laberty-Robert, C.; Calbet, J. G.; Drillon, M.; Sanchez, C.; Doudin, B.; Portehault, D. Surface-Driven Magnetotransport in Perovskite Nanocrystals. *Adv. Mater.* **2017**, *29* (9), 1604745. https://doi.org/10.1002/adma.201604745.

(16) Gonell, F.; Alem, N.; Dunne, P.; Crochet, G.; Beaunier, P.; Méthivier, C.; Montero, D.; Laberty-Robert, C.; Doudin, B.; Portehault, D. Versatile Molten Salt Synthesis of Manganite Perovskite Oxide Nanocrystals and Their Magnetic Properties. *ChemNanoMat* **2019**, *5* (3), 358–363. https://doi.org/10.1002/cnma.201800632.

(17) Gonell, F.; Sánchez-Sánchez, C. M.; Vivier, V.; Méthivier, C.; Laberty-Robert, C.; Portehault, D. Structure–Activity Relationship in Manganese Perovskite Oxide Nanocrystals from Molten Salts for Efficient Oxygen Reduction Reaction Electrocatalysis. *Chem. Mater.* **2020**, *32* (10), 4241–4247. https://doi.org/10.1021/acs.chemmater.0c00681.

(18) Gu, W.; Song, Y.; Liu, J.; Wang, F. Lanthanum-Based Compounds: Electronic Band-Gap-Dependent Electrocatalytic Materials for Oxygen Reduction Reaction. *Chem. Eur. J.* **2017**, *23* (42), 10126–10132. https://doi.org/10.1002/chem.201701136.

(19) Weber, M. L.; Lole, G.; Kormanyos, A.; Schwiers, A.; Heymann, L.; Speck, F. D.; Meyer, T.; Dittmann, R.; Cherevko, S.; Jooss, C.; Baeumer, C.; Gunkel, F. Atomistic Insights into Activation and Degradation of $La_{0.6}Sr_{0.4}CoO_3$ Electrocatalysts under Oxygen Evolution Conditions. *J. Am. Chem. Soc.* **2022**, *144* (39), 17966–17979.

(20) Gholizadeh, A.; Malekzadeh, A.; Ghiasi, M. Structural and Magnetic Features of $La_{0.7}Sr_{0.3}Mn_{1-x}Co_xO_3$ Nano-Catalysts for Ethane Combustion and CO Oxidation. *Ceram. Int.* **2016**, *42* (5), 5707–5717. https://doi.org/10.1016/j.ceramint.2015.12.101.

(21) Yang, Y.; Wang, Y.; Xiong, Y.; Huang, X.; Shen, L.; Huang, R.; Wang, H.; Pastore, J. P.; Yu, S. H.; Xiao, L.; Brock, J. D.; Zhuang, L.; Abruña, H. D. *In Situ* X-Ray Absorption Spectroscopy of a Synergistic Co-Mn Oxide Catalyst for the Oxygen Reduction Reaction. *J. Am. Chem. Soc.* **2019**, *141* (4), 1463–1466. https://doi.org/10.1021/jacs.8b12243.

(22) Kyômen, T.; Yamazaki, R.; Itoh, M. Correlation between Magnetic Properties and Mn/Co Atomic Order in $LaMn_{0.5}Co_{0.5}O_{3+\delta}$: I. Second-Order Nature in Mn/Co Atomic Ordering and Valence State. *Chem. Mater.* **2003**, *15* (25), 4798–4803. https://doi.org/10.1021/cm0302781.

(23) Joy, P. A.; Khollam, Y. B.; Date, S. K. Spin States of Mn and Co in LaMn0.5Co0.5. *Phys Rev B* **2000**, *62* (13), 8608–8610. https://doi.org/10.1103/PhysRevB.62.8608.

(24) Pecchi, G.; Campos, C.; Peña, O.; Cadus, L. E. Structural, Magnetic and Catalytic Properties of Perovskite-Type Mixed Oxides $LaMn_{1-y}Co_yO_3$ (y=0.0, 0.1, 0.3, 0.5, 0.7, 0.9, 1.0). *J. Mol. Catal. A Chem.* **2008**, *282* (1–2), 158–166. https://doi.org/10.1016/j.molcata.2007.12.022.

(25) Celorrio, V.; Calvillo, L.; Granozzi, G.; Russell, A. E.; Fermin, D. J. $AMnO_3$ (A = Sr, La, Ca, Y) Perovskite Oxides as Oxygen Reduction Electrocatalysts. *Top. Catal.* **2018**, *61* (3–4), 154–161. https://doi.org/10.1007/s11244-018-0886-5.

(26) Xu, X.; Pan, Y.; Zhong, Y.; Shi, C.; Guan, D.; Ge, L.; Hu, Z.; Chin, Y. Y.; Lin, H. J.; Chen, C. te; Wang, H.; Jiang, S. P.; Shao, Z. New Undisputed Evidence and Strategy for Enhanced Lattice-Oxygen Participation of Perovskite Electrocatalyst through

Cation Deficiency Manipulation. *Adv. Sci.* **2022**, *9* (14), 2200530. https://doi.org/10.1002/ADVS.202200530.

(27) Tofield, B. C.; Scott, W. R. Oxidative Nonstoichiometry in Perovskites, an Experimental Survey; the Defect Structure of an Oxidized Lanthanum Manganite by Powder Neutron Diffraction. *J. Solid State Chem.* **1974**, *10* (3), 183–194. https://doi.org/https://doi.org/10.1016/0022-4596(74)90025-5.

(28) Varela, M.; Oxley, M. P.; Luo, W.; Tao, J.; Watanabe, M.; Lupini, A. R.; Pantelides, S. T.; Pennycook, S. J. Atomic-Resolution Imaging of Oxidation States in Manganites. *Phys. Rev. B* **2009**, *79* (8), 85117. https://doi.org/10.1103/PhysRevB.79.085117.

(29) Wang, Z. L.; Yin, J. S.; Jiang, Y. D. EELS Analysis of Cation Valence States and Oxygen Vacancies in Magnetic Oxides. *Micron* **2000**, *31* (5), 571–580. https://doi.org/https://doi.org/10.1016/S0968-4328(99)00139-0.

(30) Cortés-Gil, R.; Hernando, A.; Alonso, J. M.; Sigcho-Villacís, K. M.; Azor-Lafarga, A.; Martínez, J. L.; Ruiz-González, M. L.; González-Calbet, J. M. Novel Insights into the Magnetic Behavior of Non-Stoichiometric $LaMnO_{3+\delta}$ Nanoparticles. *J. Mater. Chem. C* **2021**, *9* (32), 10361–10371. https://doi.org/10.1039/D0TC05972B.

(31) Reller, A.; Thomas, J. M.; Jefferson, D. A.; Uppal, M. K. Superstructures Formed by the Ordering of Vacancies in a Selective Oxidation Catalyst: Grossly Defective $CaMnO_3$. *Proc. R. Soc. Lond. A* **1984**, *394*, 223–241. https://doi.org/https://doi.org/10.1098/rspa.1984.0077.

(32) Alonso, J. M.; Cortés-Gil, R.; Ruiz-González, L.; González-Calbet, J. M.; Hernando, A.; Vallet-Regí, M.; Dávila, M. E.; Asensio, M. C. Influence of the Synthetic Pathway on the Properties of Oxygen-Deficient Manganese-Related Perovskites. *Eur. J. Inorg. Chem.* **2007**, *2007* (21), 3350–3355. https://doi.org/https://doi.org/10.1002/ejic.200700108.

(33) Cortés-Gil, R.; Ruiz-González, M. L.; Alonso, J. M.; Vallet-Regí, M.; Hernando, A.; González-Calbet, J. M. Ferromagnetism in a New Manganese-Related Brownmillerite: $La_{0.5}Sr_{0.5}MnO_{2.5}$. *Chem. Eur. J.* **2007**, *13* (15), 4246–4252. https://doi.org/https://doi.org/10.1002/chem.200601279.

(34) Hagenmuller, P.; Pouchard, M.; Grenier, J. C. Nonstoichiometry in the Perovskite-Type Oxides: An Evolution from the Classical Schottky-Wagner Model to the Recent High Tc Superconductors. *Solid State Ionics* **1990**, *43*, 7–18. https://doi.org/https://doi.org/10.1016/0167-2738(90)90464-3.

(35) Mastin, J.; Einarsrud, M.-A.; Grande, T. Structural and Thermal Properties of $La_{1-x}Sr_xCoO_{3-\delta}$. *Chem. Mater.* **2006**, *18* (25), 6047–6053. https://doi.org/10.1021/cm061539k.

(36) Hansteen, O. H.; Bréard, Y.; Fjellvåg, H.; Hauback, B. C. Divalent Manganese in Reduced $LaMnO_{3-\delta}$ – Effect of Oxygen Nonstoichiometry on Structural and Magnetic Properties. *Solid State Sci.* **2004**, *6* (3), 279–285. https://doi.org/https://doi.org/10.1016/j.solidstatesciences.2004.01.002.

(37) Pishahang, M.; Bakken, E.; Stølen, S.; Larring, Y.; Thomas, C. I. Oxygen Non-Stoichiometry and Redox Thermodynamics of $LaMn_{1-x}Co_xO_{3-\delta}$. *Solid State Ionics* **2013**, *231*, 49–57. https://doi.org/https://doi.org/10.1016/j.ssi.2012.10.009.

(38) Risch, M. Perovskite Electrocatalysts for the Oxygen Reduction Reaction in Alkaline Media. *Catalysts* **2017**, *7* (5), 154. https://doi.org/10.3390/catal7050154.

(39) Fabbri, E.; Nachtegaal, M.; Binninger, T.; Cheng, X.; Kim, B. J.; Durst, J.; Bozza, F.; Graule, T.; Schäublin, R.; Wiles, L.; Pertoso, M.; Danilovic, N.; Ayers, K. E.; Schmidt, T. J. Dynamic Surface Self-Reconstruction Is the Key of Highly Active Perovskite Nano-Electrocatalysts for Water Splitting. *Nat. Mater.* **2017**, *16* (9), 925–931. https://doi.org/10.1038/nmat4938.

(40) Li, H.; Chen, Y.; Seow, J. Z. Y.; Liu, C.; Fisher, A. C.; Ager, J. W.; Xu, Z. J. Surface Reconstruction of Perovskites for Water Oxidation: The Role of Initial Oxides' Bulk Chemistry. *Small Science* **2022**, *2* (1), 2100048. https://doi.org/10.1002/smsc.202100048.

(41) Mefford, J. T.; Rong, X.; Abakumov, A. M.; Hardin, W. G.; Dai, S.; Kolpak, A. M.; Johnston, K. P.; Stevenson, K. J. Water Electrolysis on $La_{1-x}Sr_xCoO_{3-\delta}$ Perovskite Electrocatalysts. *Nat. Commun. 2016 7:1* **2016**, *7* (1), 1–11. https://doi.org/10.1038/ncomms11053.

(42) Moysiadou, A.; Lee, S.; Hsu, C. S.; Chen, H. M.; Hu, X. Mechanism of Oxygen Evolution Catalyzed by Cobalt Oxyhydroxide: Cobalt Superoxide Species as a Key Intermediate and Dioxygen Release as a Rate-Determining Step. *J. Am. Chem. Soc.* **2020**, *142* (27), 11901–11914. https://doi.org/10.1021/jacs.0c04867.

(43) Weatherup, R. S.; Wu, C. H.; Escudero, C.; Pérez-Dieste, V.; Salmeron, M. B. Environment-Dependent Radiation Damage in Atmospheric Pressure X-Ray Spectroscopy. *J. Phys. Chem. B* **2018**, *122* (2), 737–744. https://doi.org/10.1021/acs.jpcb.7b06397.

(44) Risch, M.; Stoerzinger, K. A.; Han, B.; Regier, T. Z.; Peak, D.; Sayed, S. Y.; Wei, C.; Xu, Z.; Shao-Horn, Y. Redox Processes of Manganese Oxide in Catalyzing Oxygen Evolution and Reduction: An *in Situ* Soft X-Ray Absorption Spectroscopy Study. *J. Phys. Chem. C* **2017**, *121* (33), 17682–17692. https://doi.org/10.1021/acs.jpcc.7b05592.

(45) Gorlin, Y.; Chung, C. J.; Nordlund, D.; Clemens, B. M.; Jaramillo, T. F. Mn_3O_4 Supported on Glassy Carbon: An Active Non-Precious Metal Catalyst for the Oxygen Reduction Reaction. *ACS Catal.* **2012**, *2* (12), 2687–2694. https://doi.org/10.1021/cs3004352.

(46) Gorlin, Y.; Lassalle-Kaiser, B.; Benck, J. D.; Gul, S.; Webb, S. M.; Yachandra, V. K.; Yano, J.; Jaramillo, T. F. *In Situ* X-Ray Absorption Spectroscopy Investigation of a Bifunctional Manganese Oxide Catalyst with High Activity for Electrochemical Water Oxidation and Oxygen Reduction. *J. Am. Chem. Soc.* **2013**, *135* (23), 8525–8534. https://doi.org/10.1021/ja3104632.

(47) Kern, J.; Chatterjee, R.; Young, I. D.; Fuller, F. D.; Lassalle, L.; Ibrahim, M.; Gul, S.; Fransson, T.; Brewster, A. S.; Alonso-Mori, R.; Hussein, R.; Zhang, M.; Douthit, L.; de Lichtenberg, C.; Cheah, M. H.; Shevela, D.; Wersig, J.; Seuffert, I.; Sokaras, D.; Pastor, E.; Weninger, C.; Kroll, T.; Sierra, R. G.; Aller, P.; Butryn, A.; Orville, A. M.; Liang, M.; Batyuk, A.; Koglin, J. E.; Carbajo, S.; Boutet, S.; Moriarty, N. W.; Holton, J. M.; Dobbek, H.; Adams, P. D.; Bergmann, U.; Sauter, N. K.; Zouni, A.; Messinger, J.; Yano, J.; Yachandra, V. K. Structures of the Intermediates of Kok's Photosynthetic Water Oxidation Clock. *Nature* **2018**, *563* (7731), 421–425. https://doi.org/10.1038/s41586-018-0681-2.

(48) He, X.; Yin, F.; Li, G. A Co/Metal–Organic-Framework Bifunctional Electrocatalyst: The Effect of the Surface Cobalt Oxidation State on Oxygen Evolution/Reduction Reactions in an Alkaline Electrolyte. *Int. J. Hydrogen Energy* **2015**, *40* (31), 9713–9722. https://doi.org/10.1016/j.ijhydene.2015.06.027.

(49) Rong, X.; Parolin, J.; Kolpak, A. M. A Fundamental Relationship between Reaction Mechanism and Stability in Metal Oxide Catalysts for Oxygen Evolution. *ACS Catal.* **2016**, *6* (2), 1153–1158.

(50) Surendranath, Y.; Kanan, M. W.; Nocera, D. G. Mechanistic Studies of the Oxygen Evolution Reaction by a Cobalt-Phosphate Catalyst at Neutral pH. *J. Am. Chem. Soc.* **2010**, *132* (46), 16501–16509.

(51) Watanabe, M.; Okunishi, E.; Ishizuka, K. Analysis of Spectrum-Imaging Datsets in Atomic-Resolution Electron Microscopy. *Microscopy and Analysis* **2009**, *23*, 5–7.

(52) Lassalle-Kaiser, B.; Gul, S.; Kern, J.; Yachandra, V. K.; Yano, J. In Situ/Operando Studies of Electrocatalysts Using Hard X-Ray Spectroscopy. *J. Electron Spectrosc. Relat. Phenom.* **2017**, *221*, 18–27. https://doi.org/10.1016/j.elspec.2017.05.001.

TOC

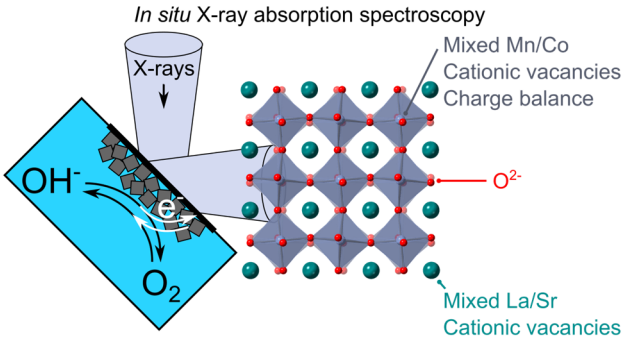
In situ X-ray absorption spectroscopy
X-rays
OH-
e-
O2
Mixed Mn/Co
Cationic vacancies
Charge balance
O2-
Mixed La/Sr
Cationic vacancies

Supporting information

Tuning of Oxygen Electrocatalysis in Perovskite Oxide Nanoparticles by the Cationic Composition

Madeleine Han[1,2], Isabel Gómez-Recio,[2] Daniel Gutiérrez Martín,[3] Nathaly Ortiz Peña,[4] Maria Luisa Ruiz-González,[3] Mohamed Selmane,[5] José M. González-Calbet,[3] Ovidiu Ersen,[4] Andrea Zitolo[1], Benedikt Lassalle-Kaiser*[1], David Portehault*[2], Christel Laberty-Robert*[2]

[1] Synchrotron SOLEIL, L'Orme des Merisiers, Départementale 128, 91190, Saint-Aubin, France

[2]Sorbonne Université, CNRS, Laboratoire Chimie de la Matière Condensée de Paris, LCMCP, 4 Place Jussieu, F-75005 Paris, France

[3] Dpto. de Química Inorgánica I, Facultad de Ciencias Químicas, Universidad Complutense, 28040 Madrid, Spain

[4]Institut de Physique et Chimie des Matériaux de Strasbourg (IPCMS), UMR 7504 CNRS − Université de Strasbourg, 23 rue du Loess, BP 43, Strasbourg Cedex 2, France

[5] Sorbonne Université, CNRS, Institut des Matériaux de Paris-Centre, FR2482, F-75005, Paris France

Benedikt Lassalle-Kaiser benedikt.lassalle@synchrotron-soleil.fr

Christel Laberty-Robert christel.laberty@sorbonne-universite.fr

David Portehault david.portehault@sorbonne-universite.fr

Materials characterization

Table S-1. Composition of the samples **LMCO30** and **LMCO40** determined by WDXRF and by Rietveld refinement of powder XRD patterns.

Sample	Co/Mn (WDXRF at. ratio)	La/(Mn+Co) (WDXRF at. ratio)	$La(OH)_3$/perovskite (WDXRF wt. ratio)	$La(OH)_3$/perovskite (Rietveld wt. ratio)
LMCO30	0.34	1.1	10	17
LMCO40	0.49	1.1	11	20

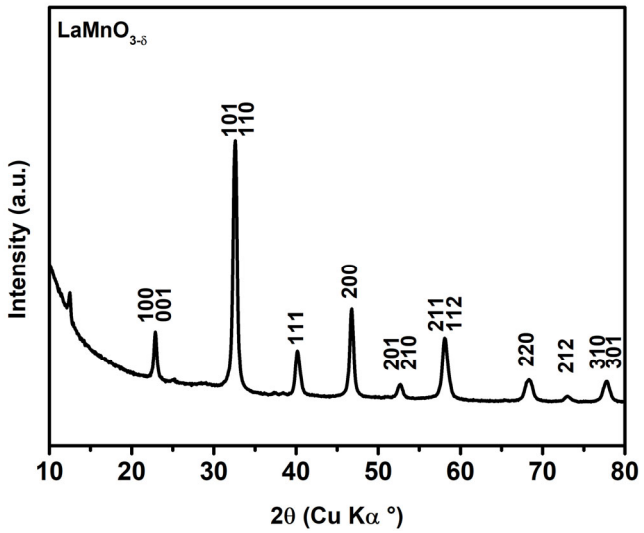

Figure S-1. Powder XRD pattern of the **LMO** sample.

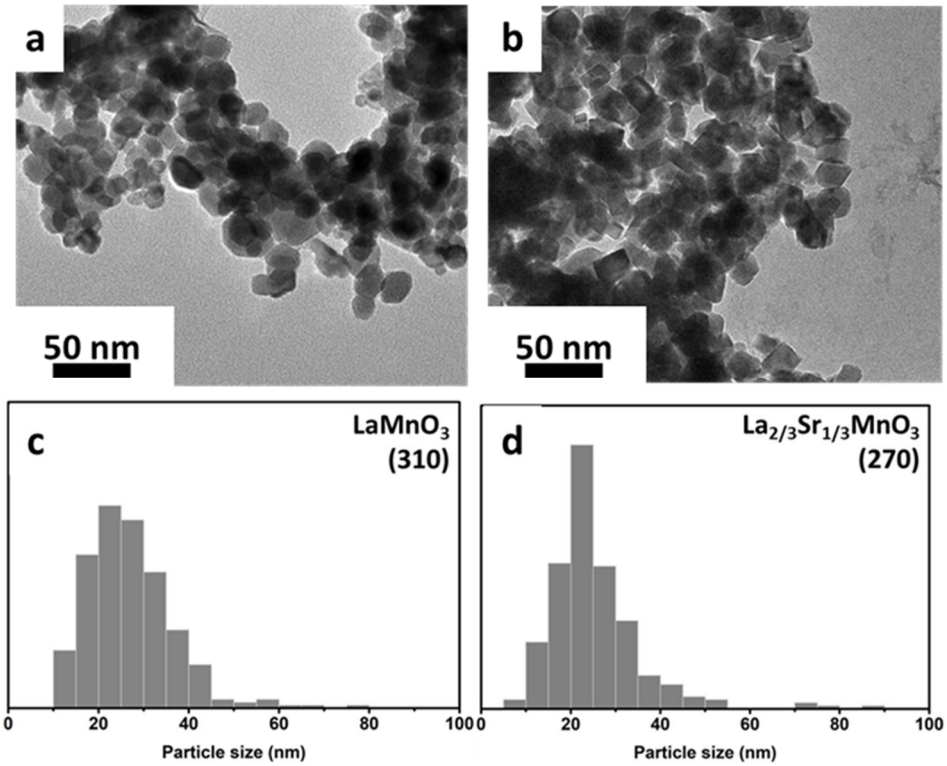

Figure S-2. TEM images of (a) **LMO** and (b) **LSMO** and their (c and d) respective diameter distribution (numbers between brackets are the number of particles counted).

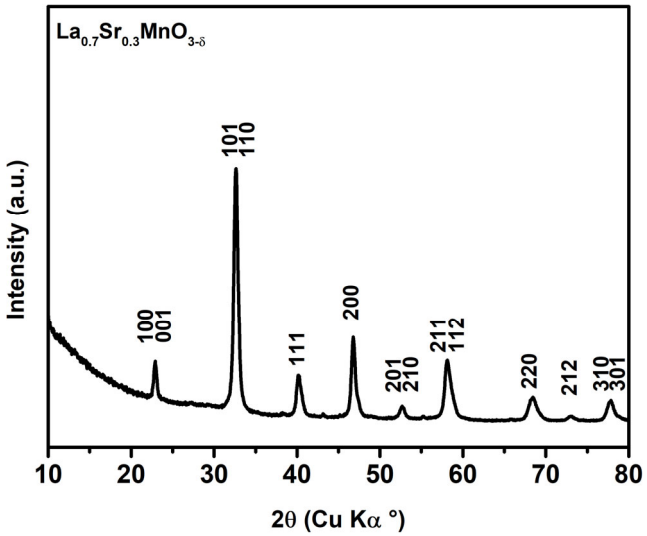

Figure S-3. Powder XRD pattern of the **LSMO** sample.

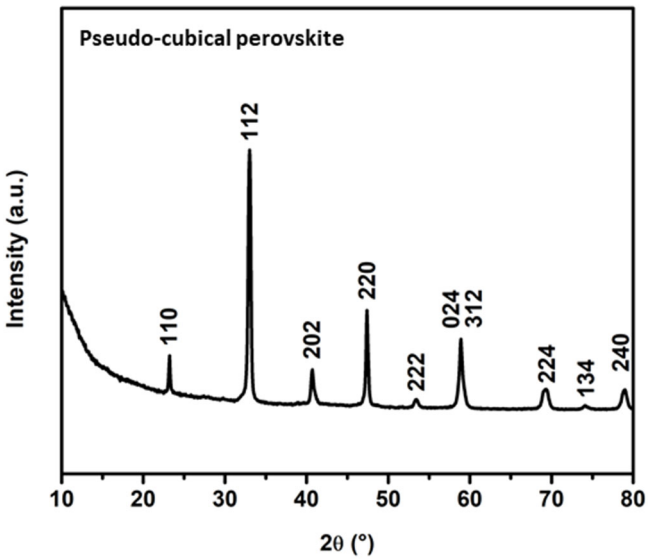

Figure S-4. Powder XRD pattern of the **LSCO** sample.

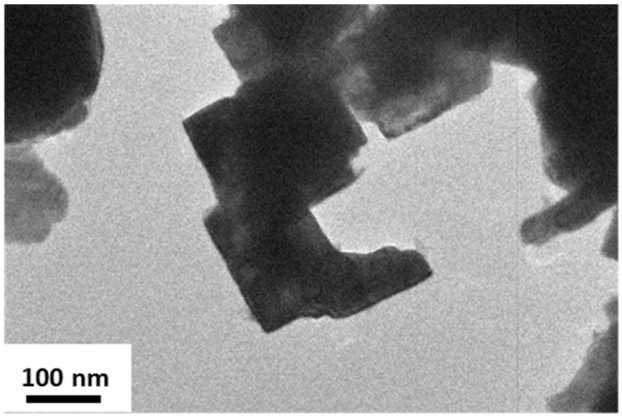

Figure S-5. TEM image of the **LSCO** sample.

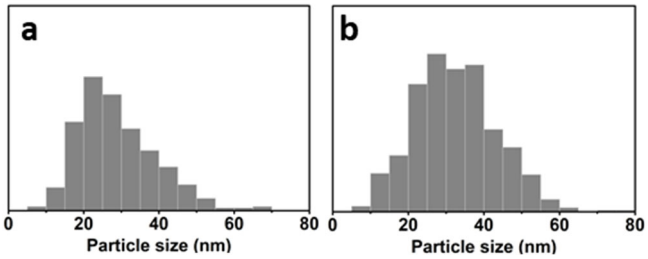

Figure S-6. Diameter distribution of (a) **LMCO30** and (b) **LMCO40**.

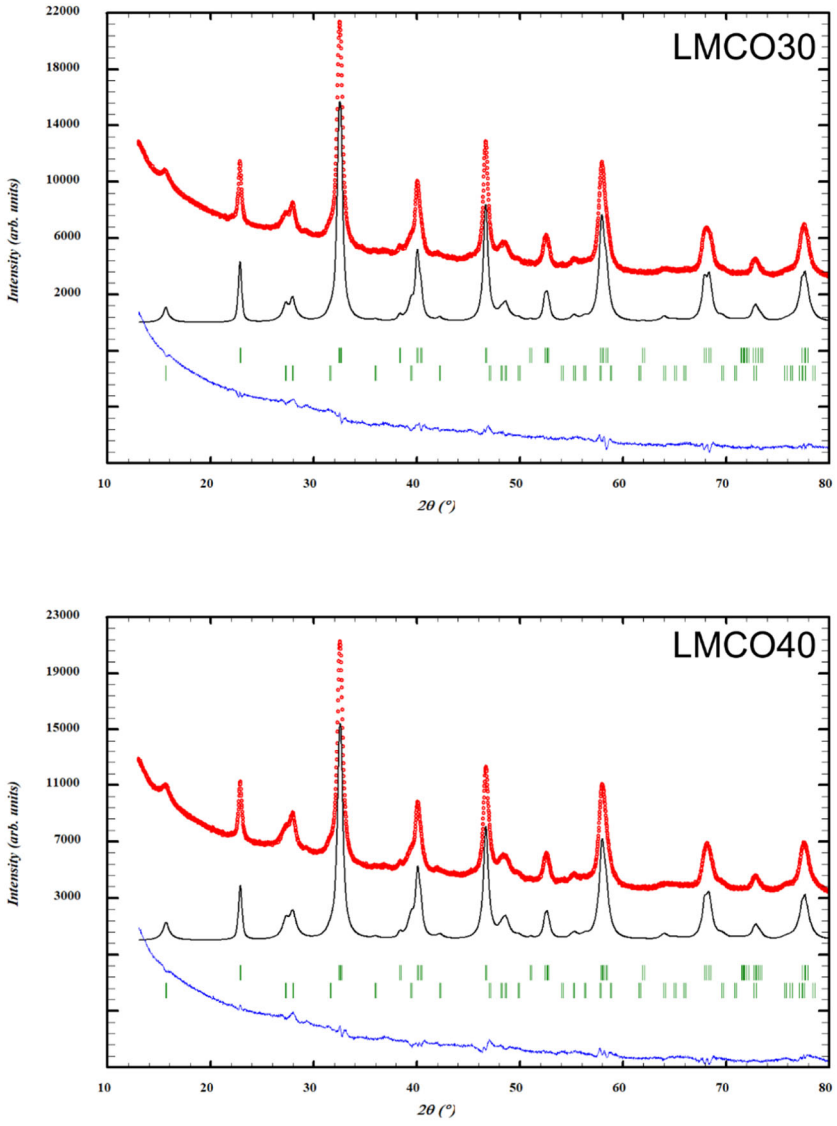

Figure S-7. Rietveld refinement of the powder XRD patterns of **LMCO30** and **LMCO40** samples. The patterns were refined using the Rietveld method as implemented in the DDM, Derivative Difference Minimization program (R_{DDM} = 8.05% and 8.36% for **LMCO30** and **LMCO40**, respectively),[1] by using as initial parameters the reference PDF+4 cards 04-023-5052 (SG *R-3C*) and 00-036-1481 for the perovskite and $La(OH)_3$ phases, respectively. The refined lattice parameters of the perovskites are $a = b = 5.5180(6)$ Å, c = 13.396(3) Å and $a = b = 5.5167(7)$ Å, c = 13.409(3) Å, for **LMCO30** and **LMCO40**, respectively, in full agreement with the expected perovskite structure. The weight ratio $La(OH)_3$/perovskite evaluated from the Rietveld analysis is 17 and 20 wt. ratio (**Table S-1**). These values are slightly higher than those expected from elemental WDXRF analysis (**Table S-1**). This discrepancy is attributed to the uncertainties in the evaluation of compositions from XRD and WDXRF, which amount to few percents for each technique. We note that this do not rule out the possible presence of amorphous Mn and Co-rich phases, although such components could not be detected by TEM and the *in situ* behaviour we observed by XAS, with constant Mn/Co oxidation state during electrocatalysis, cannot be ascribed to such phases, which on the opposite undergo changes of redox states during electrocatalysis.[2] Likewise, Co_3O_4 was implemented in the Rietveld analysis, but no corresponding peak could be detected and the fit was not improved by adding this third phase, so that we discard the presence of the spinel at amounts above the detection threshold of powder XRD.

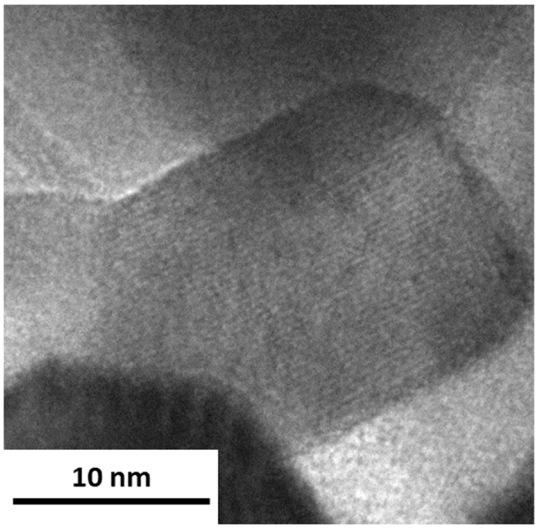

Figure S-8. HRTEM image of **LMCO40**, showing the single crystal character of a nanoparticle.

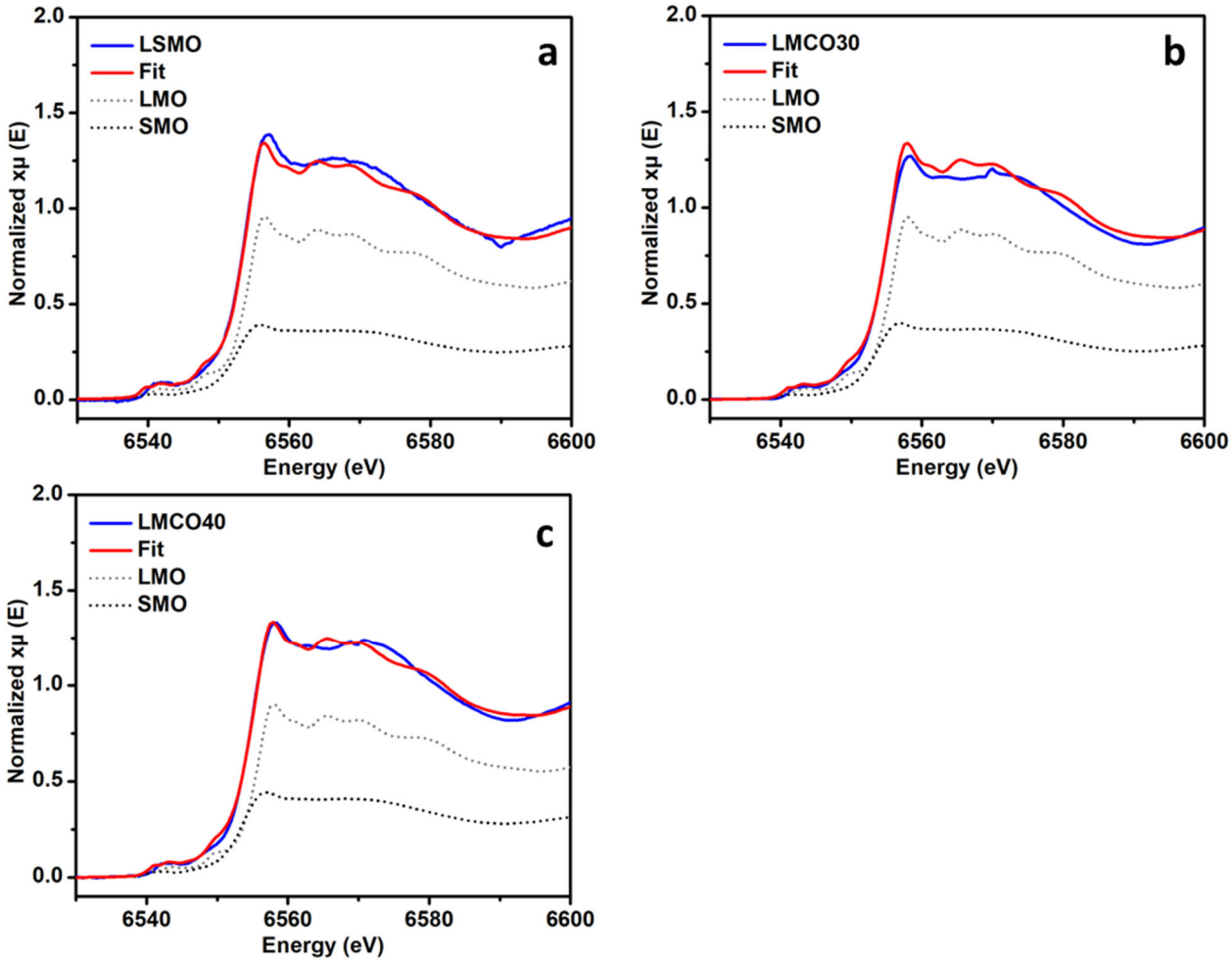

Figure S-9. XANES linear combination fitting (LCF) of (a) **LSMO**, (b) **LMCO30** and (c) **LMCO40**. The reference XAS spectrum of **SMO** is taken from Celorrio *et al.*[4]

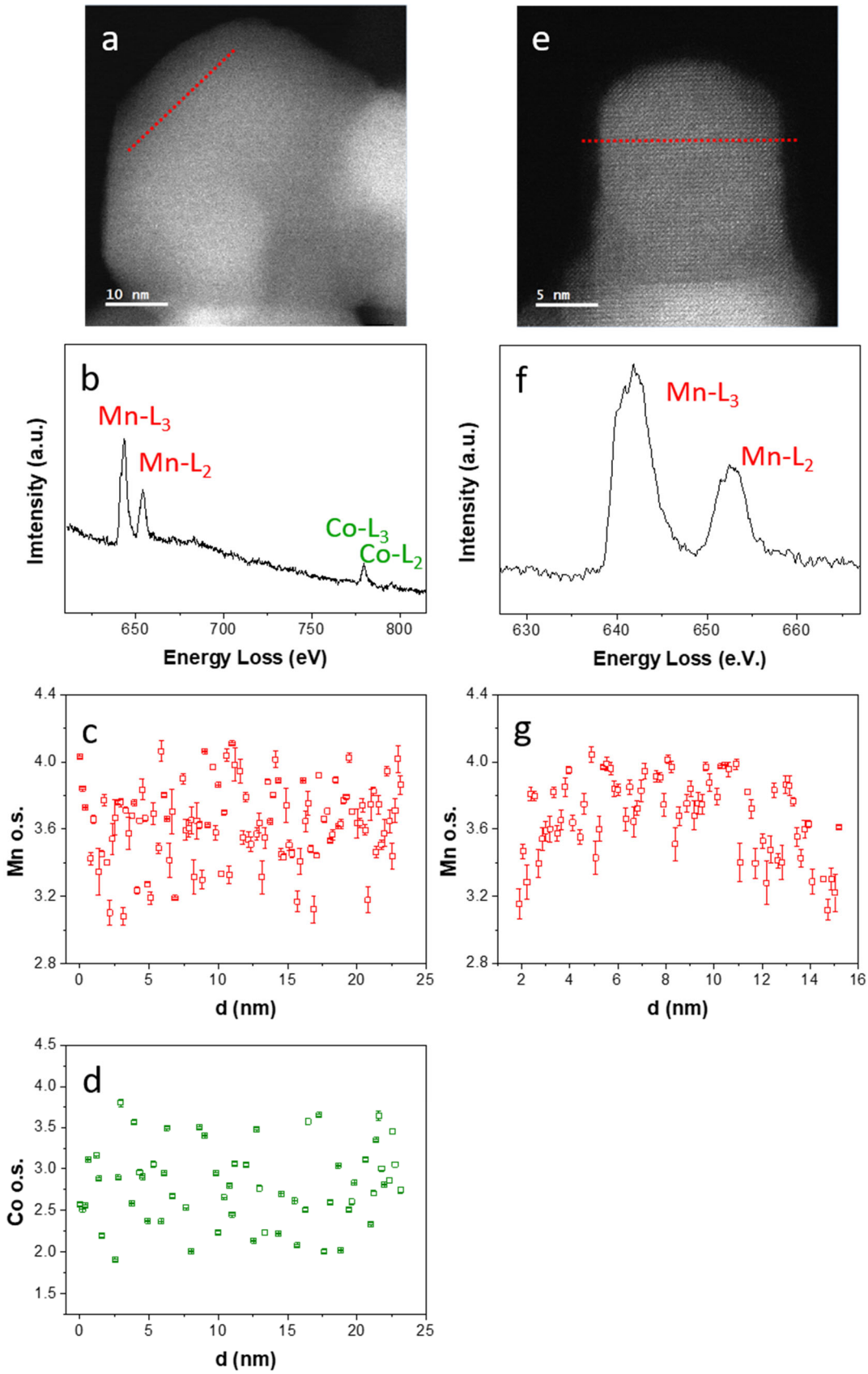

Figure S-10. STEM study of (a-d) **LMCO30** and (e-g) **LMO**. HAADF-STEM images of (a) **LMCO30** and (e) **LMO**. The dashed lines are those used for recorded the corresponding EELS sum spectra (b, f). (c,g) Mn and (d) Co oxidation states evaluated along the analysis lines shown in (b,f).

Table S-1. Oxidation state of transition metals in perovskites calculated by XANES and STEM-EELS and chemical composition determined by STEM-EDX. STEM-EELS and STEM-EDX measurements were performed on single particles to ensure the homogeneity of the compositions.

	XANES		EELS		EDX			
Sample	**Mn**	**Co**	**Mn**	**Co**	**La**	**Sr**	**Mn**	**Co**
LMO	3.0	N/A	N/A	N/A				
LSMO	3.4±0.1	N/A	3.6±0.1	N/A	37.0	16.0	46.9	
LSCO	N/A	3.2	N/A	N/A				
LMCO30	3.6±0.2	2.6	3.7±0.2	2.6±0.3	50.2		36.6	12.85
LMCO40	3.5±0.2	2.6	3.7±0.2	2.8±0.1	48.9		34.8	16.21

Table S-3. Anionic (x) and cationic (γ) stoichiometries for **LMO**, **LSMO**, **LSCO** and **LMCO40** in the pristine state and in ORR and OER conditions, considering cationic (x=3-δ, $ABO_{3-\delta}$) or anionic ($(AB)_\gamma O_3$) lattices fully occupied, respectively. The highlighted cells correspond to the most likely compositions, reported in **Table 1** of the main text.

	Pristine		OCV		ORR		OER	
	ABO_x	**$(AB)_\gamma O_3$**	**ABO_x**	**$(AB)_\gamma O_3$**	**ABO_x**	**$(AB)_\gamma O_3$**	**ABO_x**	**$(AB)_\gamma O_3$**
Sample	x	γ	x	γ	x	γ	x	γ
LMO	3.00	1.00	2.90	1.00	2.70	1.11	2.95	1.02
LSMO	3.05	0.98	3.00	0.98	2.75	1.09		
LSCO	2.98	1.01	2.93	1.03	2.83	1.49	2.98	1.01
LMCO40	3.16	0.95	3.12	0.95	3.12	0.96	3.12	0.96

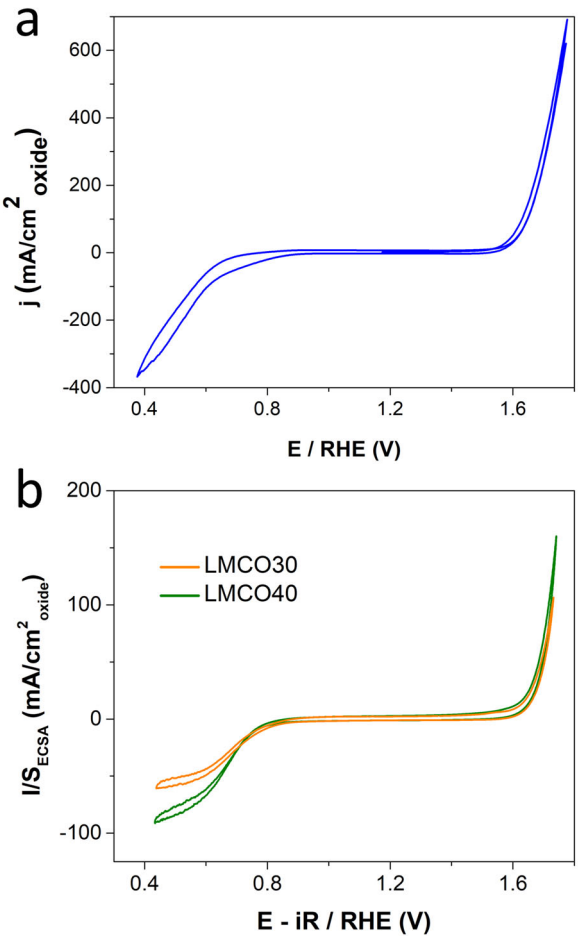

Figure S-11. (a) *Ex situ* cyclic voltammogram of **LSCO** in an O_2-saturated 0.1 M KOH electrolyte using a rotating disk electrode (1600 rpm) at 10 $mV \cdot s^{-1}$. Electrocatalyst loading: 30 $\mu g \cdot cm^{-2}_{disk}$. The current has been normalized *versus* the BET surface area. (b) *Ex situ* cyclic voltammograms of mixed B-site perovskites **LMCO30** and **LMCO40** normalized *versus* the measured electrochemical surface area (ECSA = 106 and 59 cm^2_{oxide}/cm^2_{RDE} for **LMCO30** and **LMCO40**, respectively, by assuming a specific capacitance of 40 $\mu F\ cm^2_{oxide}$ ^{2}) recorded at the same loading, rotation speed and with the same electrolyte. For the measurements in this last graph, an additional step has been added to prepare the ink before deposition: after mixing the components, the ink has been roll milled overnight at 60 rpm in a vial filled with zirconium beads (diameter 2 mm, mass ratio catalyst/zirconium = 0.02 %).

Table S-4. BET specific surface area of the pristine samples.

	LMO	**LMCO30**	**LMCO40**	**LSMO**	**LSCO**
BET surface area ($m^2\ g^{-1}$)	**35**	**35**	**35**	**35**	**16**

Table S-5. Oxidation states interpolated from the edge energies measured *operando* at half-edge jump of the Mn and Co K-edges in **LMO**, **LSMO**, **LSCO** and **LMCO40** in ORR and OER conditions.

	Pristine		**OCV pH=13**		**ORR (0.4 V/RHE)**		**OER (1.8 V/RHE)**	
Sample	**Mn**	**Co**	**Mn**	**Co**	**Mn**	**Co**	**Mn**	**Co**
LMO	3.0	N/A	2.8	N/A	2.4	N/A	2.9	N/A
LSMO	3.4	N/A	3.3	N/A	2.8	N/A	-	N/A
LSCO	N/A	3.2	N/A	3.1	N/A	2.9	N/A	3.2
LMCO40	3.5	2.6	3.4	2.6	3.4	2.6	3.4	2.6

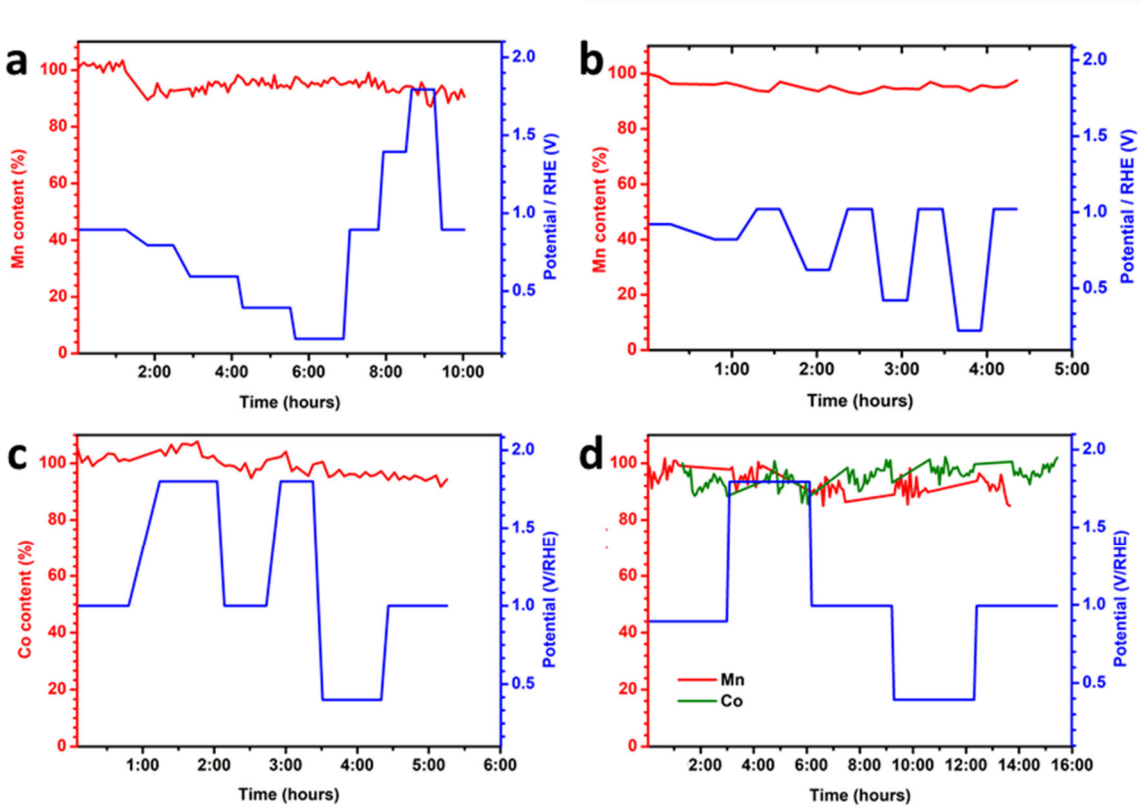

Figure S-12. Non-normalized *operando* XANES spectra of (a) **LMO** (Mn-K), (b) **LSMO** (Mn-K), (c) **LSCO** (Co-K) and (d) **LMCO40** (Mn-K in red and (Co-K in green) during ORR and OER experiments. The dissolution of Mn and Co are investigated by measuring the intensity of the XAS edge before normalization, as it is directly correlated to the concentration of the excited element. The monitored edge height is calculated as the difference between the intensity before the edge (*ca.* 6500 and 7700 eV for Mn and Co respectively) and after the edge (*ca.* 6800 or 7800 eV for Mn and Co respectively). In **figure S-11**, the edge intensity is given as percentage of the intensity of the first XAS measured in the electrolyte, *ie.* the first OCV.

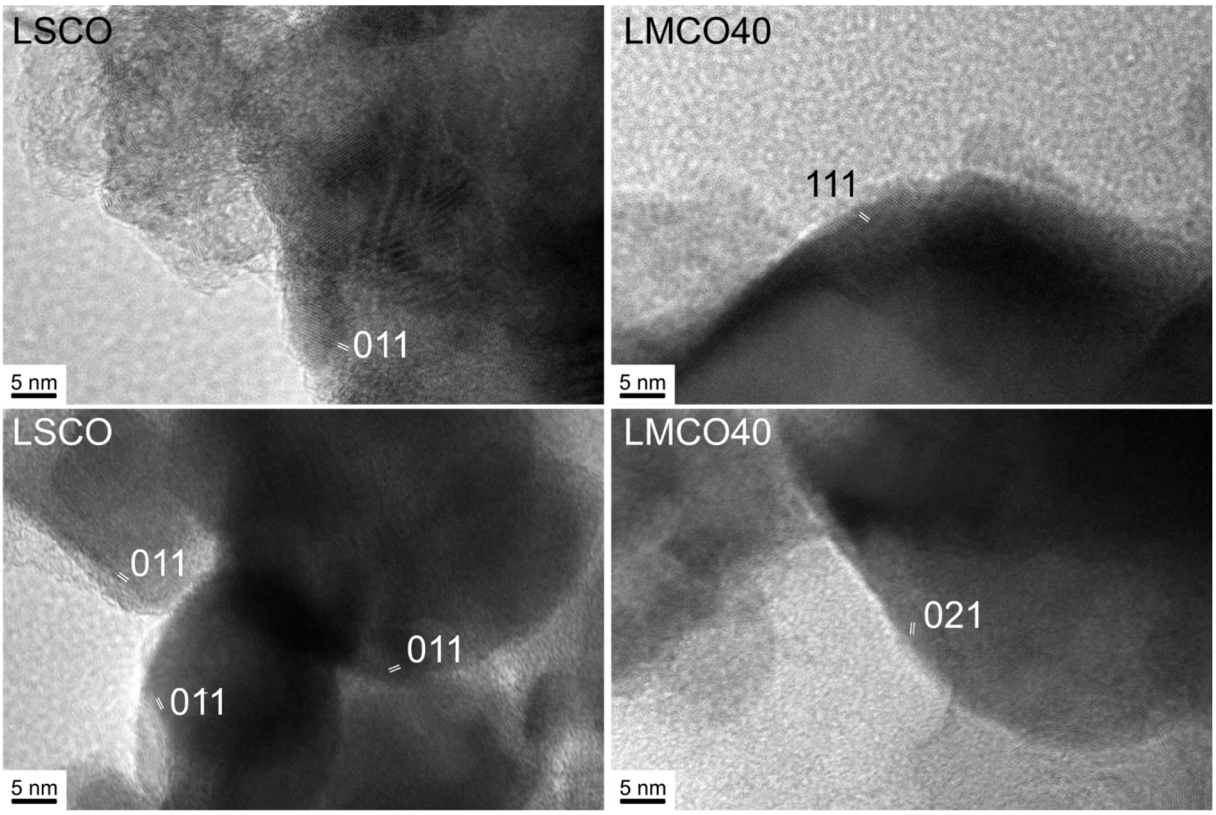

Figure S-13. HRTEM images of LSCO and LMCO40 samples after 200 CVs between 0.4 and 1.7 V *vs* RHE in a 01 M KOH aqueous electrolyte.

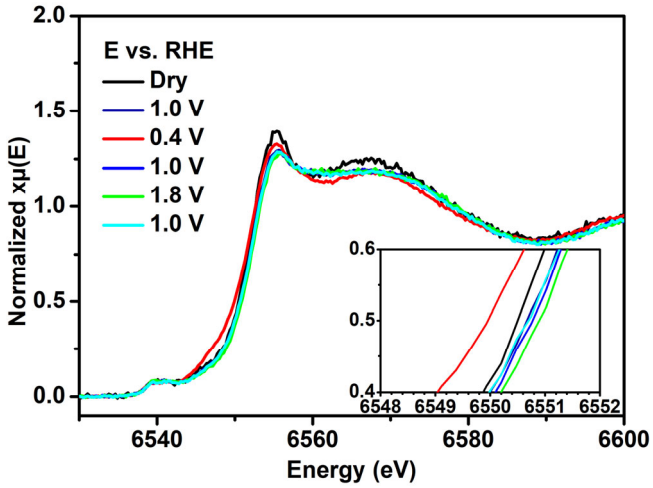

Figure S-14. *Operando* XANES spectra of **LMO** during ORR and OER experiment. Dry electrode is in black. Successive potentials are applied: 1.0 (dark blue), 0.4 (red), 1.0 (blue), 1.8 (green) and 1.0 V/RHE (cyan). In the frame is a zoom at the half-jump area.

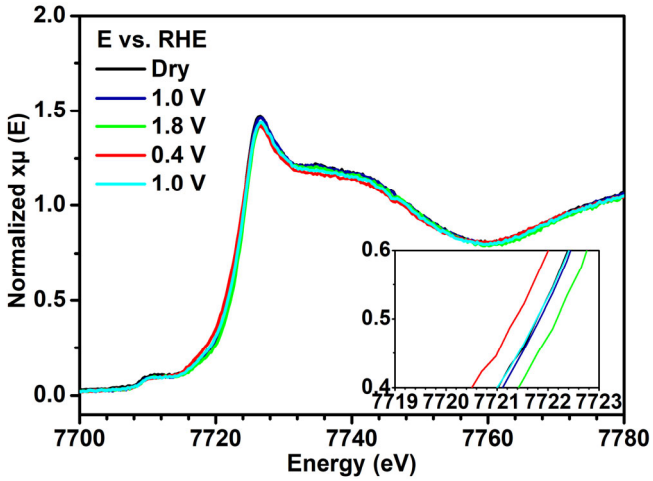

Figure S-15. *Operando* XANES spectra of **LSCO** during ORR and OER experiment. Dry electrode is in black. Successive potentials are applied: 1.0, 1.8, 0.4 and 1.0 V/RHE. In the frame is a zoom at the half-jump area.

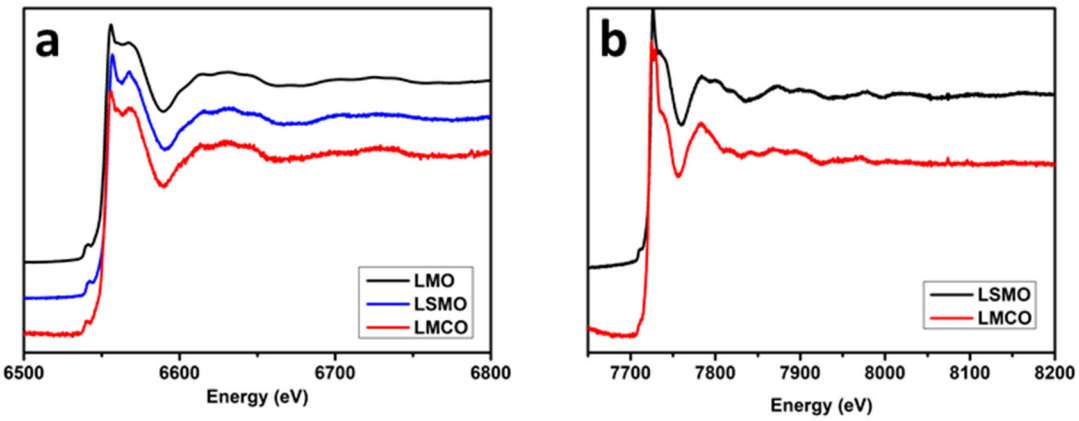

Figure S-16 *Operando* XANES (a) at the Mn K-edge of **LMO**, **LSMO** and **LMCO40** and (b) at the Co K-edge of **LSCO** and **LMCO40** at the open circuit voltage.

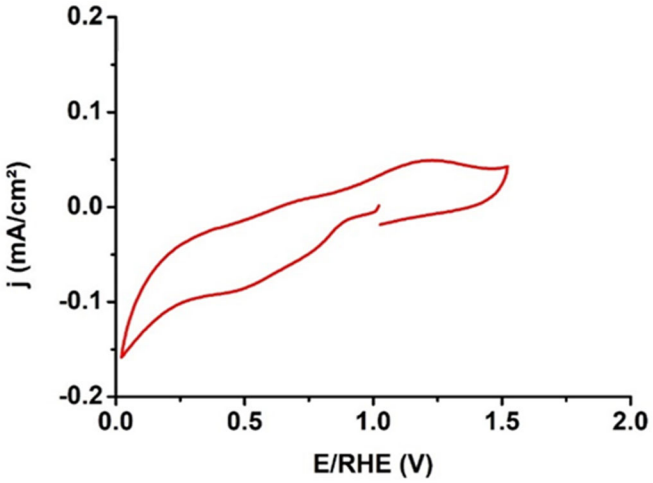

Figure S-17. Control cyclic voltammogram of **LMO** in an O_2-saturated KOH 0.1 M electrolyte during the *operando* experiment. Scan rate: 100 $mV \cdot s^{-1}$.

Table S-6. *Operando* study of **LMO**. Potential of each steps and the number of scans acquired. No potential was applied during the steps in blue.

Potential (V/RHE)	Dry	OCV	0.8	0.6	0.4	0.2	0.9	1.4	1.8	0.9
Scans	16	16	9	16	16	16	16	8	8	8

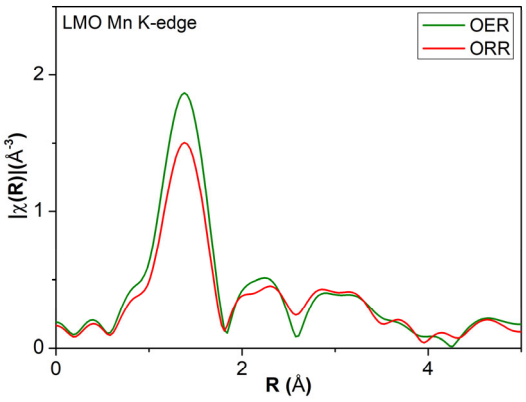

Figure S-18. FT-EXAFS at the Mn K-edge of **LMO** during OER (1.8 V/RHE) and ORR (0.4 V/RHE).

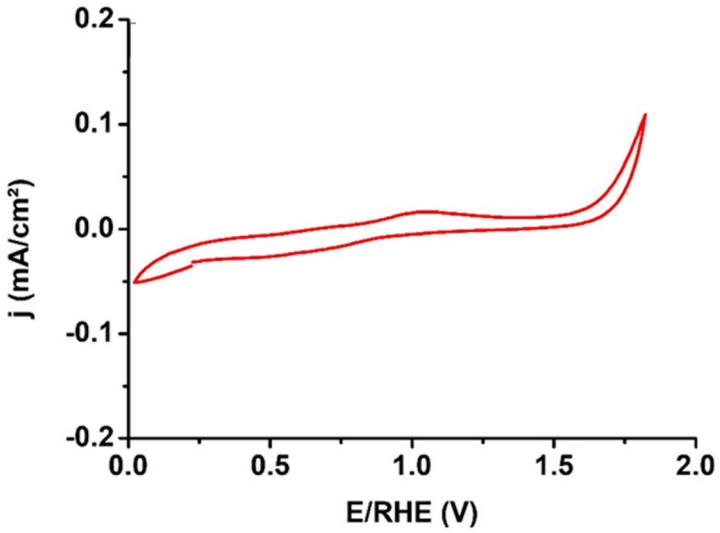

Figure S-19. Control cyclic voltammograms of **LSMO** in O_2-saturated KOH 0.1 M solution during the *operando* experiment. Scan rate: 100 $mV \cdot s^{-1}$

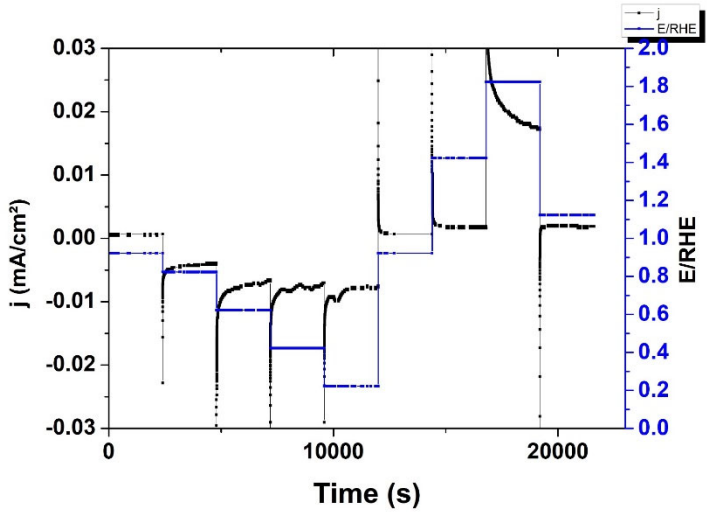

Figure S-20. Chronoamperogram of **LSMO** in an O_2-saturated KOH 0.1 M solution during the *operando* experiment.

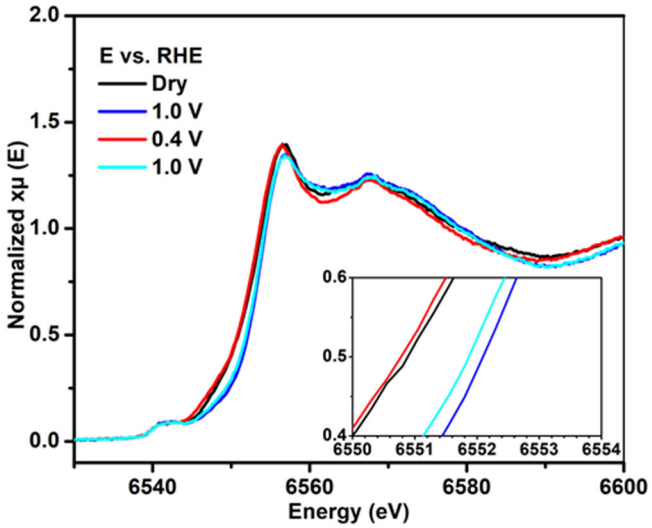

Figure S-21. *Operando* XANES spectra of **LSMO** during ORR and OER experiment. Dry electrode is in black. Successive potentials are applied: 1.0, 0.4, 1.0 V/RHE. In the frame is a zoom at the half-jump area.

Table S-7. *Operando* study of **LSMO**. Potential of each steps and the number of scans acquired. No potential was applied during the steps in blue.

Potential (V/RHE)	Dry	OCV	0.8	1.0	0.6	1.0	0.4	1.0	0.2	1.0
Scans	3	3	3	3	3	3	3	3	3	3

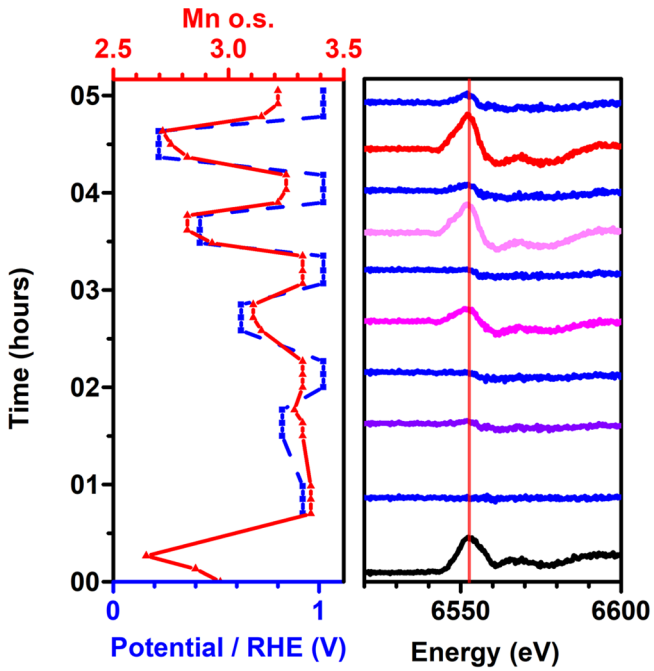

Figure S-22. Evolution of the XANES spectra and oxidation state of **LSMO** during *operando* XAS ORR experiment. Left: Time evolution of the oxidation state of Mn (red) at different potentials (blue). The oxidation state is calculated by linear interpolation from the absorption edge positions of pristine **LMO** and **SMO**. Right: XANES spectra of **LSMO** at these potentials, from which the first OCV spectrum (0.9 V/RHE) is subtracted. The red vertical line is the half-edge jump energy of the first OC spectrum.

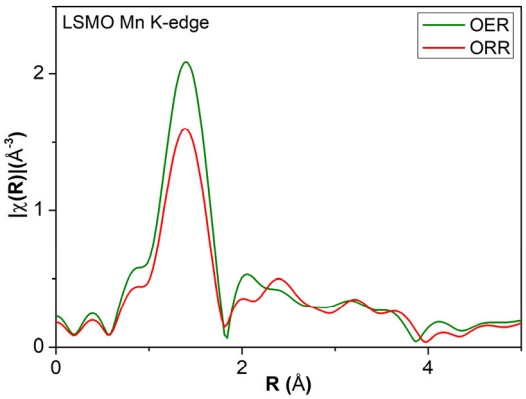

Figure S-23. FT-EXAFS at the Mn K-edge of **LSMO** during OER (1.8 V/RHE) and ORR (0.4 V/RHE).

Table S-8. LSMO during *operando* XAS ORR experiment. Oxidation state of Mn at different potentials calculated by LCF from with the reference spectra of **LMO** and **SMO**.

Potential (V /RHE)	Dry	1.0	0.8	1.0	0.6	1.0	0.4	1.0	0.2	1.0
Mn oxidation state	3.08	3.36	3.32	3.33	3.18	3.33	3.00	3.27	3.00	3.24

Table S-9. *Operando* study of **LSCO**. Potential of each steps and the number of scans acquired.

Potential (V/RHE)	Dry	OC	1.8	1.0	1.8	0.4	1.0
Scans	13	12	12	9	6	12	12

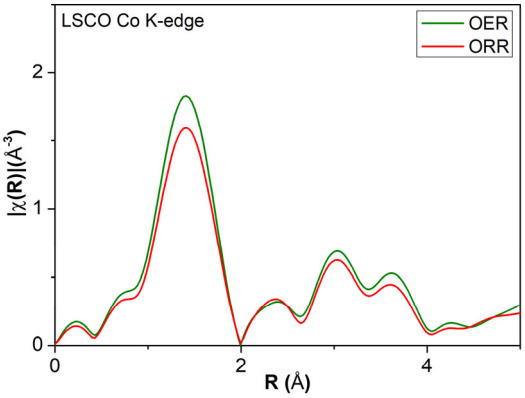

Figure S-24. FT-EXAFS at the Co K-edge of **LSCO** during OER (1.8 V/RHE) and ORR (0.4 V/RHE).

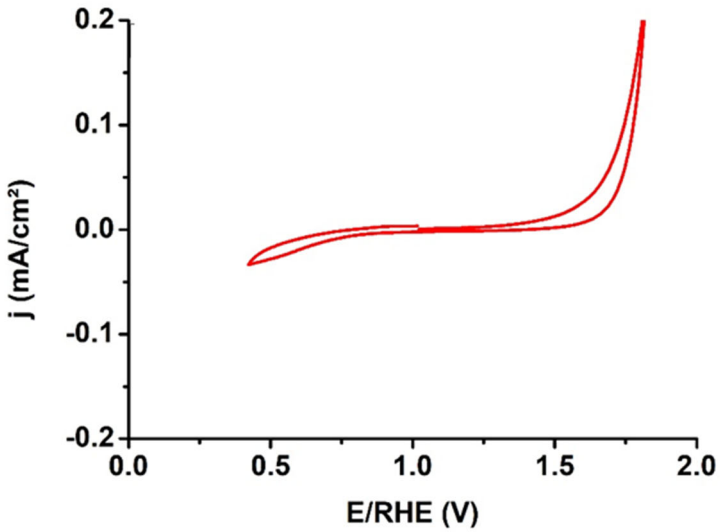

Figure S-25. Control cyclic voltammograms of **LMCO40** in O_2-saturated KOH 0.1 M solution during the *operando* experiment. Scan rate: 100 $mV \cdot s^{-1}$

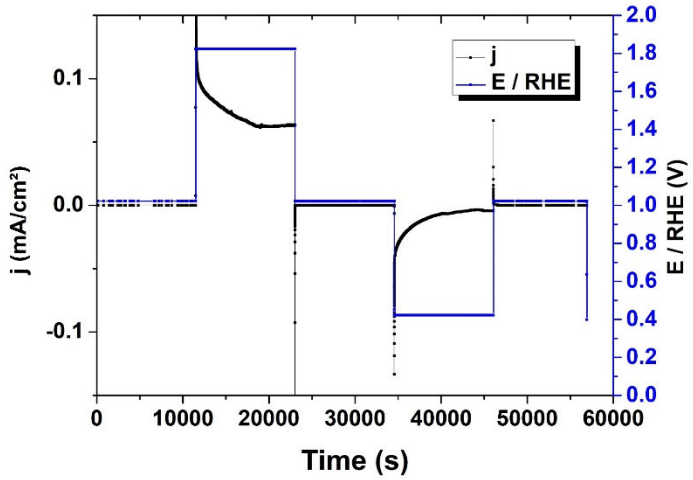

Figure S-26. Chronoamperogram of **LMCO40** in an O_2-saturated KOH 0.1 M solution during the *operando* experiment.

Table S-10. *Operando* study of **LMCO40**. Potential of each steps and the number of scans acquired.

V / RHE	Dry	Dry	OC	OC	1.8	1.8	1.0	1.0	0.4	0.4	1.0	1.0
K-Edge	Mn	Co	Mn	Co	Mn	Co	Mn	Co	Mn	Co	Mn	Co
Scans	2	4	3	6	3	6	3	6	3	6	3	6

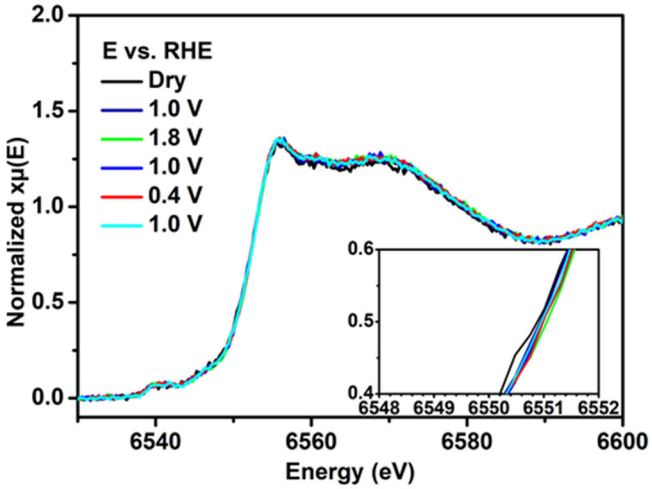

Figure S-27. *Operando* XANES spectra of **LMCO40** during OER and ORR experiment on Mn K-edge. Dry electrode is in black. Successive potentials are applied: 1.0, 1.8, 1.0, 0.4 and 1.0 V/RHE (cyan). In the frame is a zoom at the half-jump area.

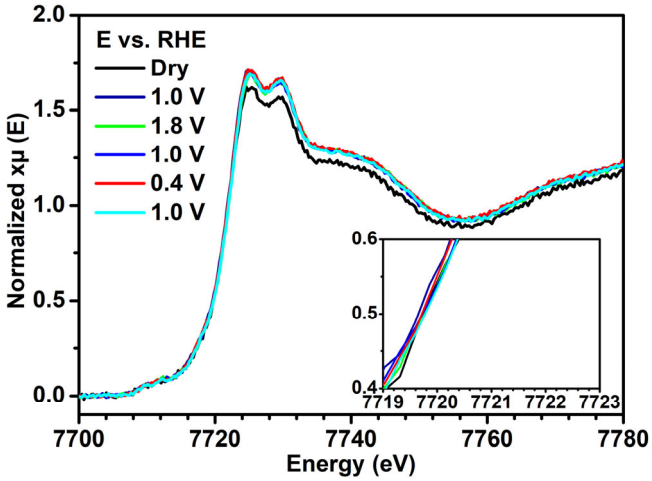

Figure S-28. *Operando* XANES spectra of **LMCO40** during OER and ORR experiment on Co K-edge. Dry electrode is in black. Successive potentials are applied: 1.0, 1.8, 0.4 and 1.0 V/RHE. In the frame is a zoom at the half-jump area.

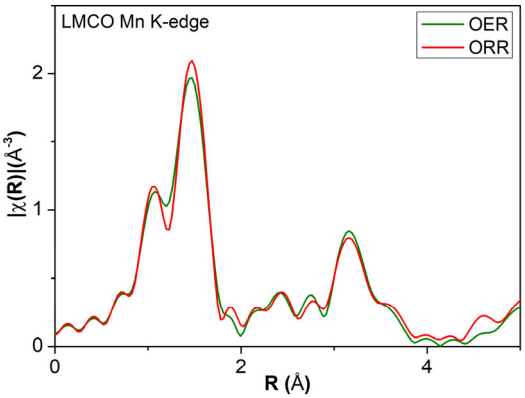

Figure S-29. FT-EXAFS at the Mn K-edge of **LMCO40** during OER (1.8 V/RHE) and ORR (0.4 V/RHE).

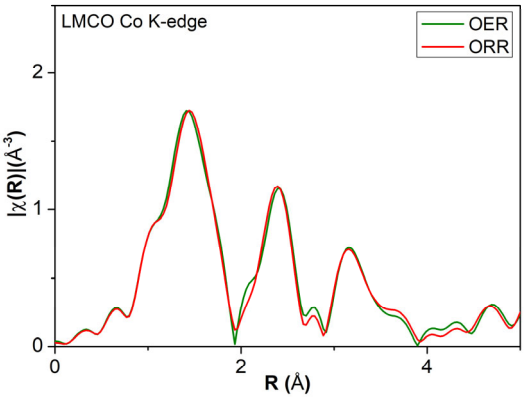

Figure S-30. FT-EXAFS at the Co K-edge of **LMCO40** during OER (1.8 V/RHE) and ORR (0.4 V/RHE).

SUPPLEMENTARY REFERENCES

(1) L. A. Solovyov, Full-profile refinement by derivative difference minimization. *J. Appl. Cryst.* **2004**, *37*, 743

(2) J. Timoshenko, B. R. Cuenya, *In Situ/Operando* Electrocatalyst Characterization by X-ray Absorption Spectroscopy. *Chem. Rev.* **2021**, *121*, 822-961.

(3) Celorrio, V.; Calvillo, L.; Granozzi, G.; Russell, A. E.; Fermin, D. J. AMnO3 (A = Sr, La, Ca, Y) Perovskite Oxides as Oxygen Reduction Electrocatalysts. *Top Catal* **2018**, *61* (3–4), 154–161.

(4) Wei, C.; Rao, R. R.; Peng, J.; Huang, B.; Stephens, I. E. L.; Risch, M.; Xu, Z. J.; Shao-Horn, Y. Recommended Practices and Benchmark Activity for Hydrogen and Oxygen Electrocatalysis in Water Splitting and Fuel Cells. *Advanced Materials* **2019**, *31* (31), 1806296.